APPLYING HIGH RESOLUTION X-RAY MICROSCOPY TO REVEAL MICROSTRUCTURAL CHANGES IN EARLY-STAGE OSTEOARTHRITIC KNEE JOINT

APPLYING HIGH RESOLUTION X-RAY MICROSCOPY TO REVEAL MICROSTRUCTURAL CHANGES IN EARLY-STAGE OSTEOARTHRITIC KNEE JOINT

By HARGHUN SINGH SOOMAL, B.H.Sc.

A Thesis Submitted to the School of Graduate Studies in Partial Fulfilment of the Requirements for the Degree of Master of Applied Science

McMaster University

Master of Applied Sciences (Biomedical Engineering)

McMaster University (2025)

Hamilton, ON, Canada

TITLE:	Applying High Resolution X-Ray Microscopy to Reveal Microstructural Changes in Early-stage Osteoarthritic Knee Joint
AUTHOR:	Harghun Singh Soomal, B.H.Sc. (McMaster University)
SUPERVISOR:	Kathryn Grandfield & Tengteng Tang
NUMBER OF PAGES:	xv, 15

Dedication

To my father, uncle, mother and sister
for my grandmother and grandfather

Thesis Lay Abstract

Knee osteoarthritis (OA) is a progressive joint disease marked by early changes in cartilage and bone that are difficult to detect using traditional imaging methods. There is a growing need for high-resolution methodologies that can capture these subtle changes at the microstructural and cellular level shedding light into how OA develops and progresses. In response to these limitations, this thesis focuses on using phase contrast high-resolution X-ray microscopy (XRM) to visualize and quantify changes in mouse knee joints following total medial meniscectomy (TMM) surgery. Utilizing this technique, this research visualizes and quantifies changes in knee tissues, emphasizing cartilage and bone cell morphology, cell volume, and how cell volume varies with tissue depth. This research provides a deeper insight into the importance of early detection and offers a more comprehensive understanding of microstructural changes during the initial stages of osteoarthritis.

Abstract

Background: In Canada, osteoarthritis affects 4 million people and costs over 1.3 billion CAD annually in joint replacements.[1] However, early detection remains a major challenge, as current clinical imaging tools cannot capture subtle tissue changes in the early stages, and the underlying mechanisms that drive disease progression are still not fully understood.[2]

Research Objectives: This thesis investigates microstructural changes in TMM-induced OA mouse models using high-resolution X-ray microscopy (XRM). It focuses on optimizing imaging and segmentation methods to assess cartilage thickness, bone architecture, and cell morphology, with the goal of improving early OA diagnostics through detailed tissue-level insights.

Methodology: 6 Male C57BL/6 mice underwent TMM on the right knee at 8 weeks old. Two weeks later, operated and control contralateral knees were EpoFix resin embedded, harvested, and then imaged with XRM. Tissue components, including articular and calcified cartilage, subchondral bone plate, cortical and trabecular bone, and osteocytes and chondrocytes, were segmented using Attention U-Net deep learning. Cartilage thickness and cell volume changes were then quantified to assess tissue degradation.

Results: High-resolution XRM analysis revealed early osteoarthritis-induced increases in osteocyte volume and altered spatial organization in the femur. Chondrocyte sphericity was preserved, but depth-dependent shifts in cell distribution were detected. Calcified cartilage thickness increased regionally, while articular cartilage and subchondral bone plate thicknesses remained stable. Bone morphometry showed subtle femoral-specific changes in cortical and trabecular regions.

Conclusions and Future Work: High-resolution XRM enabled early detection of OA-related changes in joint morphology and cell organization, including osteocyte volume, chondrocyte distribution, and articular cartilage remodeling. Future work should explore comparative segmentation tools, regional cell density, and articular cartilage surface roughness, while expanding analysis beyond the early stages to better capture site-specific adaptations and improve OA diagnostics.

Acknowledgements

I would like to express my deepest gratitude to my amazing supervisors, Dr. Tengteng Tang and Dr. Kathryn Grandfield, for introducing me to some of the most exciting and impactful areas of bone research. Your guidance and encouragement, along with your support in fostering conversations and collaborations with leading experts in biomedical and materials research, have been invaluable to my career. A special thank you to Dr. Junning Chen and Dr. Jun Zhou for providing the samples and performing the TMM surgery essential to this study.

I am sincerely grateful to my colleagues in ABB C317 and the Grandfield Research Group for their unwavering support and friendship, especially during the long hours spent together in the CCEM microscopy rooms. My sincere thanks to GRG members Nihal Ahmed, Alyssa Williams, Erica Anderson, Ryan Smith, Shane Scott, Alessandra Merlo, Blanca Keohan, Mary England, Sophia Bordignon, Jing Zhang, and Kansas Mackay for contributing to my time learning bone research, microscopy, and biomaterials.

My sincerest thanks to the technical staff at the Canadian Centre for Electron Microscopy (CCEM) who helped and advised me in completing this project. Thank you to Pardis Mohammadpour for the training and guidance on the XRM. Thank you to Celine Jacqueroud for the micro-CT advice, Jhoynner Martinez for diamond saw training & advice, and Chris Butcher for the SEM training.

Finally, I would like to thank my family, friends and mentors for their caring support and interest in my research from the start. A heartfelt thank you to my parents, Manveen and Gurjyot, whose unwavering love, support, and selflessness have been the foundation of everything I've achieved. They have always believed in me and have dedicated themselves entirely to my education and future. Their sacrifices, hard work, and commitment to my betterment have not only shaped who I am today but have also paved the way for my continued growth and success. I will be forever grateful for all they have done and continue to do for me.

Table of Content

List of Figures

List of Tables

List of All Abbreviations and Symbols

2D	Two-dimensional
3D	Three-dimensional
AC	Articular Cartilage
ACLT	Anterior Cruciate Ligament Transection
AI	Artificial intelligence
BS/TV	Bone Surface Density/Total Volume
BV/TV	Bone Volume Fraction/Total Volume
CC	Calcified Cartilage
CIA	Collagen-induced arthritis
CNN	Convolutional neural networks
Ct.Ar	Cortical Area
Ct.Po	Cortical Porosity
Ct.Th	Cortical Thickness
CT	Computed Tomography
DE-CT	Dual-energy CT
DMM	Destabilization of the Medial Meniscus
DDSA	Dodecenyl Succinic Anhydride
DMP30	2,4,6-Tri(dimethylaminomethyl)phenol
Micro-CT	Micro-computed Tomography
MMP-13	Metalloproteinases
MRI	Magnetic Resonance Imaging
NMA	Nadic Methyl Anhydride
PB-PC	Propagation Based Phase Contrast
ROI	Region of Interest
SCBP	Subchondral Bone Plate
SDD	Source-to-Detector Distance
SMI	Structure Model Index
Tb. N	Trabecular Number
Tb.Sp	Trabecular Separation
Tb.Th	Trabecular Thickness
TMM	Total Medial Meniscectomy
Tt.Ar	Total Area
VEGF	Vascular endothelial growth factor
VLC	Visual Light Camera
XRM	X-ray Microscopy

Declaration of Academic Achievement

I confirm that the research presented in this thesis is my original work, completed independently by me, Harghun Soomal. The project was conceived by my research supervisors, Dr. Kathryn Grandfield and Dr. Tengteng Tang, who also provided guidance in interpreting the results and assisting with editing. Unless specified otherwise, I conducted all experiments, including sample preparation (stage mounting), x-ray microscopy, segmentation, quantification, and statistical analysis.

The contributions of the following researchers to the completion of this thesis are acknowledged:

1. Dr. Junning Chen (College of Engineering, Mathematics and Physical Sciences, University of Exeter, Exeter, UK.) provided the C57 mice samples and performed the embedding for the study presented in Chapter 3.
2. Dr. Jun Zhou (Biomaterials and Engineering, SHOWA University, Tokyo, Japan) performed the TMM surgery on the C57 mice samples and advised on the anatomical features investigated in the study in Chapter 3.
3. Pardis Mohammadpour (Canadian Centre for Electron Microscopy, McMaster University, Hamilton, ON) performed the phase contrast micro-CT scanning on one set of OA and control C57 mice knee sample and advised on scanning parameters in the study in Chapter 3.

Chapter 1: Introduction

1.1. Research Motivation

Osteoarthritis (OA) is a progressive, degenerative joint disease and one of the leading causes of disability globally, affecting over 300 million people worldwide and approximately 4 million individuals in Canada alone.[3] The socioeconomic burden of OA is substantial, with annual healthcare costs in Canada exceeding 1.3 billion CAD, largely due to joint replacement surgeries for advanced knee and hip degeneration.[4] Despite its high prevalence and impact, OA often remains undiagnosed until irreversible joint damage has occurred, primarily because current clinical tools lack the high resolution needed to detect early microstructural and cellular changes in joint tissues.

Traditional imaging modalities such as magnetic resonance imaging (MRI), computed tomography (CT), and ultrasound are widely used to assess joint health, but they offer limited resolution and contrast when it comes to capturing early-stage alterations in cartilage and bone.[5–7] These techniques often are unable to visualize and quantify articular cartilage degradation, early osteocyte and chondrocyte cell volume changes, and subtle transitions in bone architecture that precede symptomatic disease progression. As a result, individuals are typically diagnosed only after pain and mobility loss become significant, at which point the OA is often too advanced and requires surgical intervention.

Recent studies have emphasized the need for high-resolution 3D imaging approaches capable of bridging the gap between histology and clinical imaging.[8,9] Micro-computed tomography (micro-CT) has been a powerful tool in this space, particularly for bone, but remains limited in its ability to resolve soft tissues like cartilage without contrast agents.[10] Advances in synchrotron and lab-based X-ray microscopy (XRM) now offer new potential to non-destructively visualize the osteochondral interface with sub-micron resolution, enabling detailed analysis of cartilage thickness, bone microarchitecture, and even cellular morphology in 3D.[11–13] These capabilities are crucial for capturing the earliest signs of degeneration, particularly in experimental OA models where tissue remodeling can be tracked over time.

Several animal models have advanced our understanding of early osteoarthritis by enabling controlled studies before clinical symptoms appear. The destabilization of the medial meniscus (DMM) model, for instance, is widely used due to its progressive cartilage degradation and its ability to mimic OA progression following joint injury in humans.[14,15] It has helped shown progressive cartilage degradation, subchondral bone remodeling, and early osteophyte formation. Similarly, the anterior cruciate ligament transection (ACLT) model has been used to study rapid-onset OA, demonstrating alterations in subchondral bone remodeling and synovitis within weeks of injury.[16,17] The total medial meniscectomy (TMM) model is preferred for studying early-stage osteoarthritis (OA) as it provides consistent degeneration of both cartilage and subchondral bone, unlike the DMM and ACLT models, which can yield variable results and focus primarily on cartilage or

ligament damage. Therefore, TMM's comprehensive approach allows for better examination of both tissue changes and associated cellular alterations.

Nevertheless, despite advances in imaging techniques, animal models, and research within the field, there is still a gap in the ability to quantitatively assess early-stage microstructural and cellular changes in osteoarthritis (OA). Current high-resolution imaging approaches, such as X-ray microscopy (XRM), hold great promise for visualizing both cartilage and bone alterations, but challenges remain in effectively segmenting and quantifying complex 3D datasets that capture the full range of tissue and cellular variations. To address these limitations, this research is *motivated* to enhance imaging workflows and develop more robust segmentation strategies using deep learning-based approaches for XRM data. I *hypothesize* that by optimizing these segmentation methods, it will be possible to accurately capture early OA changes, including cartilage degradation, bone remodeling, and cellular changes. By systematically exploring and optimizing these methods, this work aims to provide a comprehensive framework for the accurate characterization of OA progression, ultimately improving early detection and monitoring of disease progression at the microstructural level.

1.2 Research Objectives

The overarching objective of this thesis is to characterize the microstructural and cellular alterations in mouse knee joints during OA progression using a combination of advanced imaging and deep learning-based segmentation analysis techniques. The objective is broken down into four specific subgoals schematically presented in Fig. 1-1. This research aims to:

(i) To implement deep learning-based segmentation techniques to enhance the visualization and quantification of morphological changes across joint tissues.

(ii) To assess alterations in cortical and trabecular bone, including parameters such as cortical thickness and trabecular separation.

(iii) Analyze Articular Cartilage (AC), Calcified Cartilage (CC), and Subchondral Bone Plate (SCBP) remodeling, including cartilage thickness.

(iv) To quantify cellular changes by measuring osteocyte and chondrocyte cell volume as well as changes based on cell depth dependence.

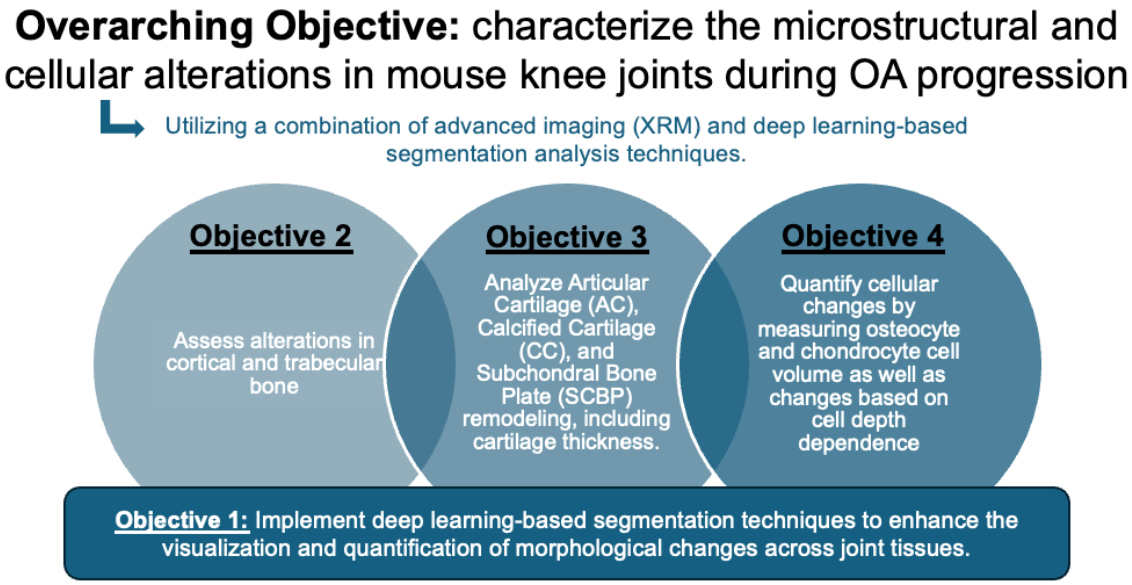

Ch. 1 – Figure 1.1. *Overview of thesis research objectives and specific subgoals presented within this thesis.*

Building on these objectives, I *hypothesize* that phase contrast X-ray microscopy (XRM) combined with deep learning-based segmentation techniques will allow for detection and quantification of early-stage microstructural and cellular changes in knee OA. Specifically, I anticipate that XRM will reveal decreased thickness in both articular and calcified cartilage, alongside increased osteocyte and chondrocyte cell volumes, which are indicative of bone remodeling and cellular hypertrophy driven by OA progression. Ultimately, these findings are expected to provide critical insights into the early structural and cellular alterations in OA, offering potential advancements for early diagnosis.

1.3 Thesis Chapter Summary

The following outlines the structure of the remaining chapters of this thesis:

Chapter 2: Literature Review. This chapter reviews relevant literature to provide context for the research and highlight key principles related to the investigation. It focuses on key aspects of osteoarthritis (OA) progression, specifically at the knee joint interface, and examines various imaging modalities such as MRI, micro-CT, CT, and ultrasound, highlighting their roles and limitations in early OA detection. Additionally, this chapter explores machine learning and deep learning models applied to the analysis of joint tissues, including articular cartilage, calcified cartilage, subchondral bone, and other key structures in OA.

Chapter 3: Materials & Methods. This chapter presents the workflow for XRM imaging of C57 mice knee joints, detailing the processes of sample cutting, embedding, fixation, mounting, scanning acquisition, and reconstruction. The established methodology provides a comprehensive approach to imaging joint tissues and lays the groundwork for further studies on OA progression using high-resolution imaging techniques.

Chapter 4: Results & Discussion. This chapter presents the analysis of the imaging results, including detailed quantification of microstructural and cellular changes observed. The findings are discussed in the context of OA progression, with a focus on cartilage thickness, bone remodeling, and cell volume changes.

Chapter 5: Conclusions & Future Work. This chapter summarizes the key findings of the research, highlighting the contributions to understanding OA progression through advanced imaging techniques. The conclusion also discusses the implications of these findings for future diagnostic approaches and suggests potential areas for further research.

Chapter 2: Background

In recent years, advancements in X-ray microscopy have opened new possibilities for investigating osteoarthritis (OA) at the microscale, particularly in visualizing complex joint structures in 3D without the need for destructive sectioning. This literature review introduces key research relevant to X-ray imaging of the knee joint, OA progression, and the osteochondral interface. The following sections are organized to cover imaging modalities, joint tissue changes, and computational segmentation approaches essential to the thesis goals of uncovering early microstructural and cellular alterations in knee OA.

2.1. Osteoarthritis (OA)

2.1.1. What is OA?

Osteoarthritis (OA) is the most common form of arthritis, defined as a degenerative joint disease characterized by progressive degradation of articular cartilage, subchondral bone remodeling, synovial inflammation, and osteophyte formation.[18] Traditionally conceptualized as a wear-and-tear disorder, OA is now widely recognized as a complex, multifactorial disease affecting the entire joint, including cartilage, bone, ligaments, menisci, and periarticular muscles.[19,20]

Globally, OA affects over 595 million people and represents the leading cause of disability in older adults.[21] The burden of OA has risen by 132% since 1990, largely due to increased life expectancy, physical inactivity, and the growing prevalence of obesity, one of the most significant modifiable risk factors.[22]

The medial tibiofemoral compartment is typically the most affected area of the knee. This is because around 75% of the knee joint's load while walking is transferred through the medial tibial plateau.[23] The uneven distribution of load between the medial and lateral compartments is a key factor in knee joint health, with this imbalance persisting even in neutral alignment and worsening in individuals with varus alignment. Varus alignment directs more load toward the medial side, significantly increasing stress on the medial compartment. This increased stress has been associated with a three- to four-fold higher risk of OA progression in the medial tibiofemoral compartment.[24] Given the critical role of the medial compartment in OA development, we have chosen to investigate the effects of total medial meniscectomy (TMM) surgery on C57BL/6 mouse knee samples. Our goal is to determine if early-stage structural changes can be detected through XRM, allowing us to explore the progression of OA at its initial stages.

2.1.2. How OA Develops & Pathogenesis

Osteoarthritis (OA) is a degenerative disease that affects the entire joint organ, including articular cartilage, subchondral bone, synovium, and periarticular structures. Its progression is driven by a complex interplay of mechanical overload, biochemical imbalances, inflammatory signaling, and cellular dysfunction that disrupts joint homeostasis.[20,25]

Cartilage Degradation and Chondrocyte Dysfunction

OA frequently begins with focal mechanical degeneration that compromise the extracellular matrix (ECM) of the articular cartilage. Chondrocytes, the primary cell type in cartilage, respond to stress and injury by shifting from a homeostatic to a catabolic phenotype, increasing the expression of matrix-degrading enzymes such as matrix metalloproteinases (MMP-13) and aggrecanases (ADAMTS-4/5), which target type II collagen and aggrecan respectively.[26–28] This imbalance between matrix synthesis and degradation leads to progressive cartilage thinning and fibrillation. Additionally, the loss of pericellular matrix integrity reduces mechanotransduction efficiency, further impairing chondrocyte function.[23]

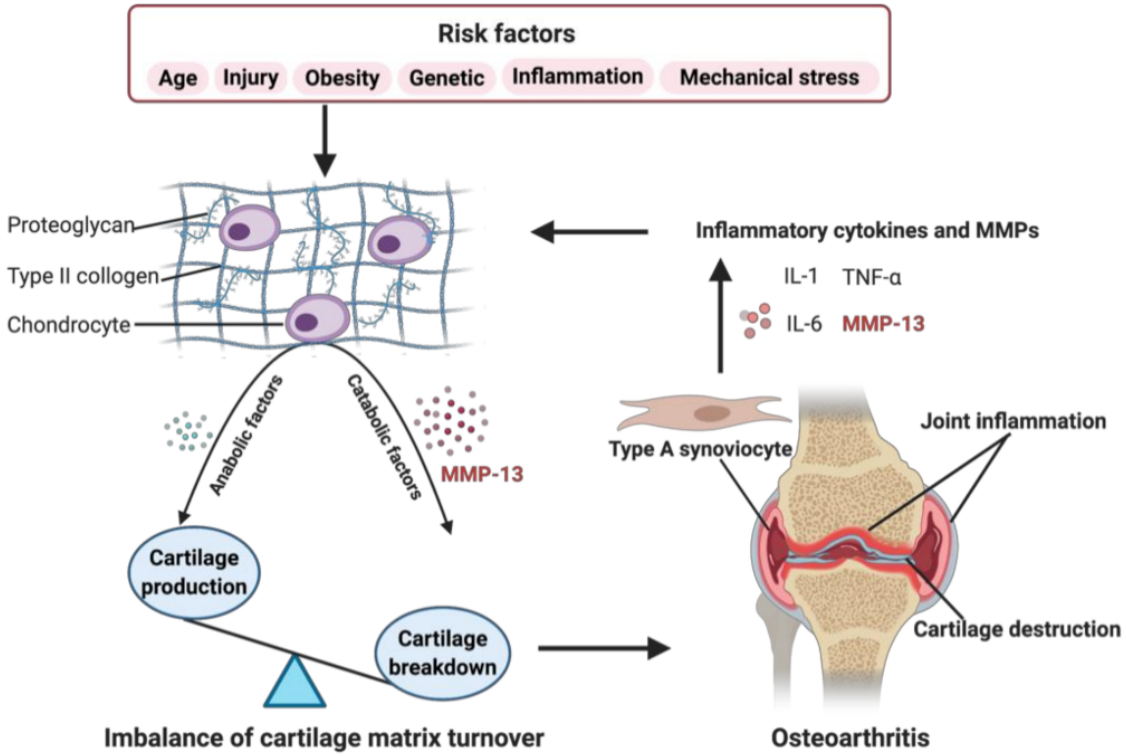

Ch. 2 – Figure 2.1. Role of MMP-13 in osteoarthritis progression. *Increased expression of MMP-13 in chondrocytes promotes type II collagen degradation, leading to cartilage breakdown and a feedback loop of inflammation and catabolic activity that accelerates OA pathology. Reproduced from Ref [29] with permission.*

Subchondral Bone Remodeling & Synovial Inflammation

Alterations in the subchondral bone are an early and persistent feature of OA. Initially, there is increased osteoclastic resorption followed by osteoblastic activity, which causes subchondral bone thickening and increased bone density.[30] These changes lead to sclerosis of the subchondral plate and trabecular disorganization, which in turn increase joint stiffness and stress on overlying cartilage, perpetuating degeneration.[31]

Synovial inflammation (synovitis) is now recognized as a critical driver of OA progression and pain.[32] Activated synoviocytes and infiltrating immune cells release pro-inflammatory cytokines (IL-1β, TNF-α), chemokines, and alarmins that exacerbate cartilage degradation and sensitize nociceptors.[33–35]

Chondrocyte Hypertrophy and Calcification

As OA progresses, surviving chondrocytes adopt a hypertrophic like phenotype, mirroring terminal differentiation seen in endochondral ossification. This includes upregulation of type X collagen, alkaline phosphatase, and vascular endothelial growth factor (VEGF), leading to cartilage mineralization and the formation of osteophytes.[36,37] Calcified cartilage expansion disrupts the osteochondral interface and contributes to impaired load distribution.

OA is not confined to cartilage. Mechanical and biochemical crosstalk among joint tissues amplifies the degenerative process. For instance, alterations in subchondral bone can alter cartilage loading and nutrient diffusion, while synovitis can amplify chondrocyte catabolism.[38] Therefore, OA should be viewed as a "whole joint disease" involving interdependent changes in bone, cartilage, and soft tissues.

2.1.3. OA Models

Preclinical models of osteoarthritis (OA) are essential for demonstrating the disease's pathophysiology and evaluating therapeutic interventions. These models aim to replicate key features of human OA, including cartilage degradation, subchondral bone remodeling, osteophyte formation, and synovial inflammation. Broadly, OA models fall into three major categories: spontaneous, chemically induced, and surgically induced.

Spontaneous models, such as aged C57BL/6 and STR/Ort mice, exhibit OA-like changes with advancing age or due to genetic predisposition. These models closely mimic the slow progression and multifactorial nature of human OA but require long experimental timelines and often show high inter-animal variability.[39] STR/Ort mice, for example, develop OA lesions as early as 20 weeks, with progressive articular cartilage degradation and subchondral bone sclerosis.[40]

Chemically induced models use agents such as monosodium iodoacetate (MIA) or collagenase to trigger cartilage degradation or joint instability. MIA models involve the intra-articular injection of MIA, which inhibits glycolysis in chondrocytes, resulting in rapid cell death and cartilage loss.[41] While these models allow for controlled induction and rapid progression, they often bypass the mechanical contributors to OA and may not fully recapitulate the structural complexity of the disease.

Surgical models are widely used due to their reproducibility and ability to mimic post-traumatic OA. These include anterior cruciate ligament transection (ACLT), destabilization of the medial meniscus (DMM), and transection medial meniscectomy (TMM). Among these, the DMM model in C57BL/6 mice is considered a gold standard for moderate OA induction, allowing for localized cartilage degeneration and osteophyte development while maintaining joint mobility.[15] The TMM model, by contrast, induces more severe and rapid joint instability, leading to pronounced degeneration of both cartilage and bone, and is often selected for studying early and aggressive tissue remodeling.[42]

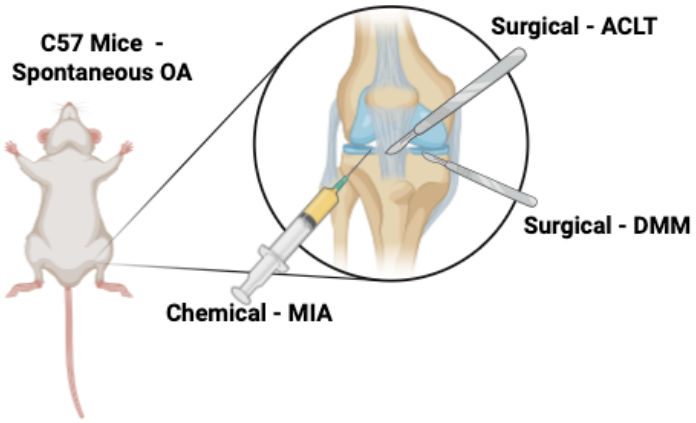

Ch. 2 – Figure 2.2. Representative OA models. *Spontaneous (e.g., STR/Ort), Chemical (MIA), and Surgical (DMM, ACLT)*

Each model has unique strengths and limitations. Spontaneous models offer translational relevance, while surgical and chemical models provide control over disease onset and severity. The selection of an appropriate model depends on the research objective, whether it is to study early-stage cellular changes, chronic progression, or therapeutic interventions.

2.2. Knee Joint Interface

2.2.1. Tissue Components

The osteochondral interface of the knee comprises a complex, multilayered structure responsible for distributing load and maintaining joint integrity. This region includes articular cartilage, calcified cartilage, the tidemark, and the subchondral bone plate, each playing a distinct mechanical and biological role.[43]

Articular Cartilage
Articular cartilage is a specialized hyaline cartilage that provides a low-friction, wear-resistant surface for joint articulation. It is avascular and relies on diffusion for nutrient exchange. Chondrocytes are the sole resident cells and are responsible for maintaining the extracellular matrix (ECM) composed of type II collagen and proteoglycans.[44] Structurally, it is organized into superficial, middle, and deep zones, each exhibiting gradients in collagen orientation, proteoglycan concentration, and cell morphology.[45,46] This zonal variation plays a crucial role in load distribution, lubrication, and resistance to mechanical forces.

Calcified Cartilage & Chondrocytes
Calcified cartilage lies between the deep zone of articular cartilage and the subchondral bone. It provides a transitional region that mechanically anchors cartilage to bone and ensures smooth stress transfer during joint loading.[47] Chondrocytes in this zone exhibit hypertrophic characteristics and reduced metabolic activity compared to those in the uncalcified zones.[48] Notably, recent work has shown that chondrocyte morphology, volume, and spatial organization change during early OA, with hypertrophy, altered depth-dependent distribution, and clustering occurring before overt matrix breakdown.[49]

These early cellular changes serve as potential indicators of joint degeneration. Investigating chondrocyte volume and distribution in calcified cartilage offers a promising approach to detect OA at pre-radiographic stages. Our study addresses this knowledge gap by quantifying cell volume and depth-dependent behavior in both femoral and tibial compartments, seeking to identify localized cellular signatures that precede tissue-level remodeling.

Subchondral Bone Plate
The subchondral bone plate lies beneath the calcified cartilage and is a metabolically active layer involved in load transmission and cartilage support. It undergoes active remodeling in OA, with early stages marked by increased porosity and reduced stiffness, and later stages characterized by sclerosis and increased thickness.[50] This altered biomechanics affects the overlying cartilage by changing the mechanical environment at the osteochondral junction.

Tidemark

The tidemark is a histological boundary separating non-calcified from calcified cartilage. It represents a mineralization front and advances during OA progression. Tidemark duplication, disruption, and vascular invasion are common in early OA and contribute to the pathological integration of calcified tissue into previously uncalcified zones.[51] These alterations may disrupt chondrocyte homeostasis and spatial organization, reinforcing the need for spatially resolved analysis across this interface.

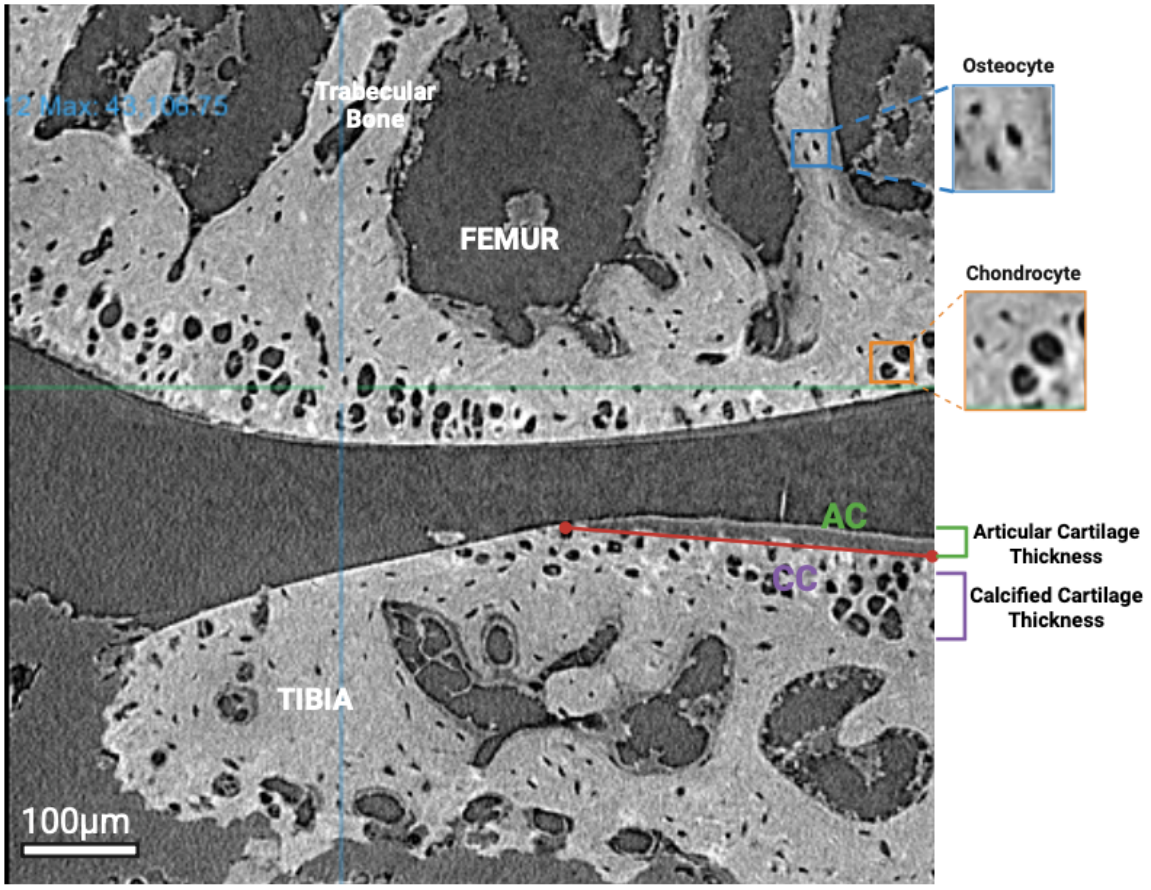

Ch. 2 – Figure 2.3. Schematic of the osteochondral interface in the knee joint. *The red line indicates the tidemark separating articular cartilage (green) from calcified cartilage (purple). The osteocyte (blue callout) and chondrocyte (orange callout) highlight key cellular components within the femur and tibia. Trabecular bone architecture is also visible within the femoral compartment.*

2.2.2. Bone & Lacunae Components

Bone's composition is categorized into three primary components: minerals, which constitute about 60% by weight; organic substances, making up 30%; and water, accounting for the remaining 10%.[52] The mineral portion is predominantly carbonated hydroxyapatite (HA), a substance that incorporates various ions, such as magnesium and strontium, exhibiting a range of compositions.[53]

Cortical Bone
Cortical bone, also referred to as compact bone, forms the dense outer shell of long bones and plays a critical role in providing mechanical strength and structural support to the joint. It is composed of tightly packed osteons, or Haversian systems, which align longitudinally along the bone axis to resist bending and torsion.[54] In the knee joint, cortical bone is most prominent in the subchondral bone plate and the metaphyseal regions of the femur and tibia.

In osteoarthritis (OA), subchondral cortical bone undergoes significant alterations that can precede or accompany cartilage degeneration. Early changes include increased bone turnover, formation of microcracks, and plate thickening, particularly in weight-bearing zones.[55,56] These changes alter load transmission across the joint, potentially exacerbating cartilage wear and joint degeneration.[50] High-resolution micro-CT studies have demonstrated that even subtle thickening or densification of the subchondral plate may reflect early-stage OA processes before macroscopic cartilage loss becomes apparent.[57]

Trabecular Bone
Trabecular, or cancellous bone, lies beneath the cortical shell and is characterized by a porous, lattice-like architecture that distributes loads and contributes to energy absorption during joint movement.[58] It is highly responsive to mechanical stimuli and undergoes continual remodeling through coordinated osteoblast and osteoclast activity.

OA-related changes in trabecular bone include decreased trabecular thickness, altered connectivity, and increased bone volume fraction, especially in advanced stages of the disease.[59] However, recent studies have shown that alterations in trabecular morphology, including changes in spacing and anisotropy, can begin during early disease progression and may be regionally specific.[60] These compartmental differences are thought to reflect shifts in localized loading patterns due to joint instability or meniscal damage.

Osteocytes
Osteocytes, the most abundant cell type in bone, reside within lacunae embedded in the mineralized matrix and form an extensive network of canaliculi for communication and mechanosensation.[61] They play a central role in coordinating bone remodeling in response to mechanical cues by regulating both osteoblast and osteoclast activity.

In the context of OA, osteocytes exhibit morphological and functional changes that may reflect early mechanical or biochemical dysregulation. Studies have shown that osteocyte lacunar density, volume, and shape are altered in OA, with signs of hypertrophy, altered sphericity, or perilacunar remodeling.[62,63] These changes are hypothesized to impact mechanotransduction and matrix homeostasis, potentially contributing to the altered bone remodeling observed in the disease. Moreover, recent high-resolution imaging techniques, such as X-ray microscopy (XRM) and synchrotron radiation micro-CT, have enabled quantification of osteocyte morphology at cellular resolution, providing a potential biomarker for early-stage OA.[64]

Investigating osteocyte morphometry and spatial distribution within cortical and trabecular compartments offers valuable insight into the microarchitectural adaptations occurring during OA progression. By correlating these changes with site-specific loading environments and cartilage status, such measurements can help identify early indicators of disease and inform mechanobiological models of joint degeneration.

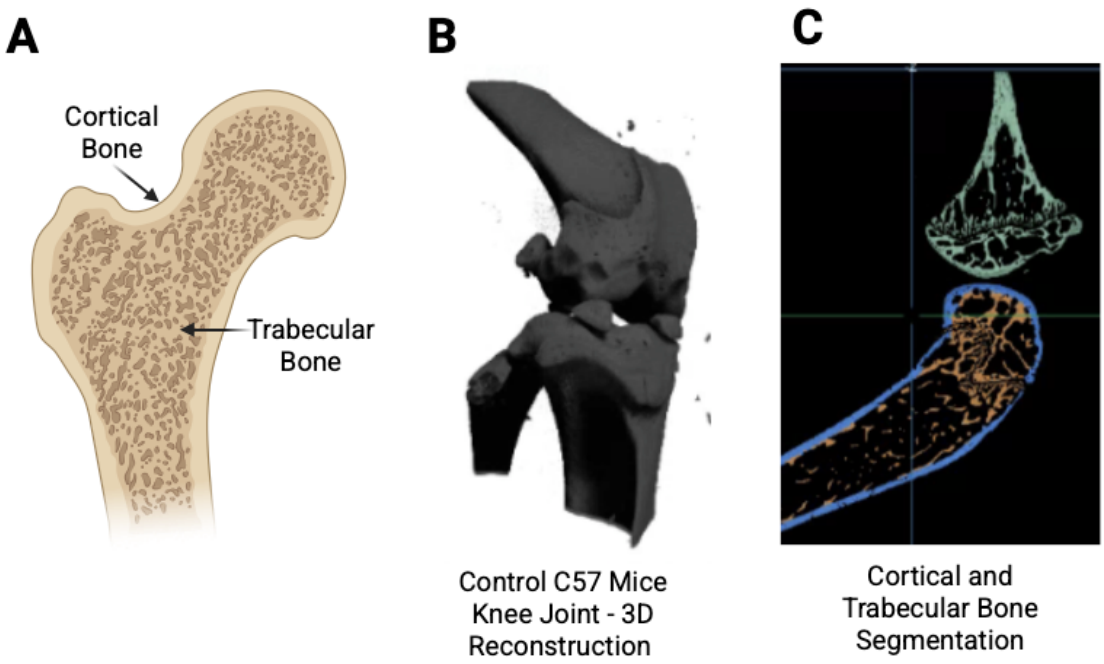

Ch. 2 – Figure 2.4. Visualization of cortical and trabecular bone compartments in the mouse knee joint. *(A) Schematic illustration of long bone structure highlighting cortical and trabecular regions. (B) 3D reconstruction of a control C57BL/6 mouse knee joint acquired using high-resolution X-ray microscopy. (C) Segmentation of cortical (blue) and trabecular (orange) bone performed in Dragonfly software.*

2.3. Imaging of Knee OA

2.3.1. Clinical Imaging

Clinical imaging plays a critical role in diagnosing and monitoring osteoarthritis (OA), yet each modality presents trade-offs in resolution, cost, and sensitivity to early-stage changes.

Magnetic resonance imaging (MRI) remains the gold standard for soft tissue assessment in OA, offering high-resolution, multiplanar views of cartilage, menisci, ligaments, and synovium.[65] Advanced MRI techniques, such as T2 mapping and delayed gadolinium-enhanced MRI of cartilage (dGEMRIC), can assess cartilage composition and detect early biochemical changes before structural damage becomes apparent.[66] However, MRI is costly, time-consuming, and may suffer from variability in interpretation and accessibility.[67]

In preclinical research, MRI has been instrumental in longitudinal studies of OA progression. For instance, Ali et al. (2018) used quantitative MRI to monitor post-traumatic OA development in a rat model following medial meniscectomy. Their study observed systematic changes in articular cartilage thickness and T2 relaxation times over eight weeks, indicating cartilage swelling and subsequent degradation. This work demonstrated MRI's usage in detecting early cartilage alterations in OA models.[68]

Similarly, a study by Luo et al. (2023) utilized diffusion–relaxation correlation spectrum imaging (DR-CSI) to detect early-stage OA in a mouse model. This technique enabled the identification of subtle changes in cartilage microstructure, highlighting MRI's potential in early OA diagnosis. However, the study also noted limitations in sensitivity and specificity, particularly in distinguishing between early degenerative changes and normal variations.[69]

Despite these advancements, MRI's application in small animal models faces challenges. The limited spatial resolution can hinder the detection of fine structural changes, and the high cost and complexity of MRI systems may restrict widespread use in preclinical studies. These limitations underscore the need for alternative imaging modalities that can provide higher resolution and more accessible assessments of early OA changes.[67]

Ultrasound, in contrast, provides real-time, cost-effective imaging of superficial joint structures, particularly the synovium and effusion.[70] While useful for guiding intra-articular injections and evaluating inflammatory components, ultrasound lacks the resolution and penetration required to assess deep cartilage or subchondral bone with sufficient precision in early OA.[71]

In preclinical models, ultrasound has shown usage in assessing synovitis and joint swelling. For example, Jia et al. (2025) employed high-frequency ultrasound to monitor joint inflammation in a collagen-induced arthritis (CIA) mouse model. Their findings

demonstrated that ultrasound could detect soft tissue thickening and joint effusion as early as seven-week post-induction, making it a useful tool for tracking inflammatory dynamics.[72]

However, the use of ultrasound in assessing certain joint structures, such as articular cartilage and subchondral bone, is limited. The technique's lower spatial resolution and limited penetration depth restrict its ability to detect early microstructural changes within cartilage layers or bone morphology, especially in small animal models.[73] Additionally, ultrasound imaging is highly operator dependent and lacks standardized protocols for cartilage thickness or osteochondral interface evaluation in rodents, making reproducibility a challenge.[74]

Computed tomography (CT) is traditionally used for evaluating bony structures, offering excellent resolution for cortical and trabecular bone morphology. While conventional CT has limited application for soft tissue imaging, advances such as dual-energy CT (DECT) and spectral CT have expanded its potential for OA assessment. These newer technologies enhance soft tissue differentiation, enabling improved visualization of cartilage, subchondral bone marrow lesions, and calcifications.[75,76]

For instance, spectral CT has been used to differentiate between healthy and degenerative cartilage based on compositional differences.[77] In a study by Zhao et al. (2023), DECT enabled detailed detection of subchondral cysts and sclerosis in patients with knee OA, offering complementary information to MRI in structural assessment.[78]

Despite these advances, CT remains suboptimal for soft tissue assessment in early OA due to its inherently low contrast resolution for non-mineralized tissues. Ionizing radiation exposure also limits its usage for longitudinal studies or pediatric populations.[65]

In conclusion, while clinical imaging tools are indispensable for evaluating moderate to advanced OA, they often fail to capture subtle microstructural and cellular changes that characterize the early disease process, highlighting the need for more sensitive modalities.

2.3.2. Pre-clinical Imaging

While clinical imaging methods provide macroscopic insight into OA pathology, they lack the resolution necessary to detect early microstructural and cellular changes. To bridge this gap, pre-clinical imaging techniques such as X-ray microscopy (XRM), Synchrotron radiation micro-computed tomography (SRμCT), and propagation-based phase contrast (PB-PC) have become essential tools in small animal models for OA research.

Synchrotron radiation micro-CT (SRμCT) remains the gold standard for bone ultrastructure imaging due to its superior flux, coherence, and energy tunability, which enable superior contrast and resolution.[79,80] These capabilities allow for detailed

visualization of osteocyte lacunae, canaliculi, and mineral density gradients, all of which are critical for understanding early osteochondral changes. For instance, Goff et al. (2021) used SRμCT to quantify osteocyte lacunar morphometry in mice and showed how age and mechanical loading affect spatial lacunar distribution and anisotropy.[81]

Despite these advantages, synchrotron-based techniques are limited by accessibility, as they require access to national or international light source facilities. This restricts their scalability for routine preclinical research, especially in studies requiring large sample cohorts or longitudinal imaging.[82]

XRM offers high-resolution, non-destructive imaging at submicron scale, making it well-suited for visualizing the joint architecture of mice. It allows for 3D quantification of key OA features such as articular cartilage thickness, subchondral bone plate remodeling, and osteocyte and chondrocyte morphology without physical sectioning.[83] Several studies have demonstrated XRM's capacity to detect and quantify early joint changes relevant to OA. Kauppinen et al. (2019) utilized contrast-enhanced XRM to map the microarchitecture of calcified cartilage and subchondral bone in human lateral tibial plateau, revealing early compartment-specific thickening that preceded overt joint degeneration.[57]

Conventional X-ray imaging relies on absorption contrast, where differences in attenuation coefficients between materials produce image contrast. However, this approach is limited when imaging soft tissues, which often have similar attenuation values due to their low atomic number (low-Z) composition. To overcome this limitation, in pre-clinical imaging has been the adoption of propagation-based phase contrast (PB-PC) to improve visualization of soft, low atomic number (low Z) materials such as cartilage and connective tissue. PB-PC imaging works by detecting X-ray phase shifts as they pass through heterogeneous structures, which are not captured by traditional absorption based techniques.[84] In PB-PC, contrast arises not from absorption, but from interference patterns generated as X-ray wavefronts propagating beyond the sample. When an object introduces phase shifts in the transmitted X-ray beam, those shifts are converted into intensity variations through free space propagation. These interference fringes become more pronounced at greater source-to-detector distances (SDD), thus enhancing the visibility of low-density features that would be invisible under standard absorption contrast. This method exploits Fresnel diffraction and does not require specialized optics or gratings, making it accessible for use with both synchrotron and high-resolution lab-based micro-CT systems.[85,86] By increasing the source-to-detector distance (SDD), image contrast is significantly enhanced, revealing subtle differences in refractive indices. This makes PB-PC ideal for resolving soft tissue interfaces, particularly within small samples like mouse knee joints, where conventional absorption contrast may fail.[87]

The key to PB-PC imaging is the detection of spatial variations in the phase of the X-ray wavefront, which correspond to gradients in the refractive index. The complex refractive index of a material is defined as $n = 1 - \delta + i\beta$, where δ represents the phase shift and β corresponds to absorption. While traditional CT is sensitive only to β, PB-PC

captures both components, with heightened sensitivity to δ in soft tissues. Because the phase shift δ is often one to two orders of magnitude larger than β in biological tissues, phase contrast imaging can reveal features such as collagen networks, cartilage layers, or cellular boundaries with significantly improved contrast.[88]

Clark et al. (2020) demonstrated that propagation-based phase contrast micro-CT allows for three-dimensional visualization and quantification of chondrocyte morphology within intact articular cartilage using a standard lab-based system, without relying on synchrotron radiation. Their approach, which involved phosphotungstic acid staining and ethanol immersion, successfully resolved individual chondrocytes and their spatial distribution in osteochondral plugs with subcellular detail, validated by histology. This non-destructive method not only captured chondrocyte density and roundness but also enabled co-visualization of subchondral bone, showing potential for comprehensive osteochondral interface imaging.[89]

2.4. Image Processing & Segmentation

Advancements in imaging resolution have created a parallel need for sophisticated image processing tools that can efficiently handle large 3D datasets and extract biologically relevant features. In OA research, segmentation workflows are essential for distinguishing between joint tissues, quantifying structural changes, and enabling cell-level analysis. This section outlines the key stages in processing X-ray microscopy (XRM) datasets, including reconstruction, visualization, and segmentation, with a focus on deep learning-based approaches.

2.4.1. Reconstruction of Data

Raw 2D projection images obtained from XRM systems are reconstructed into 3D volumetric datasets using filtered back-projection algorithms or iterative reconstruction techniques. The reconstruction process involves correction for beam hardening, flat-field normalization, ring artifact removal, and alignment, which are essential for maintaining quantitative accuracy in downstream analysis.[90,91]

2.4.2. Visualization

Following reconstruction, 3D visualization enables anatomical orientation, inspection of segmentation fidelity, and qualitative interpretation of the dataset. Software platforms such as **ORS Dragonfly**, Avizo, and Fiji are commonly used for volume rendering, multi-planar reconstructions (MPR), and surface generation.[92]

Dragonfly in particular offers novel interactive 3D visualization combined with quantitative tools for measuring thickness, object counts, and spatial relationships. Orthogonal views in axial, sagittal, and coronal planes are used to validate tissue

boundaries and cell segmentations. Proper visualization is critical for annotation, segmentation quality control, and figure preparation.

2.4.3. Deep Learning Models

Manual segmentation of high-resolution 3D datasets is time-consuming and subject to inter-operator variability. Deep learning-based models have emerged as powerful alternatives, offering automation, scalability, and enhanced feature recognition. Convolutional neural networks (CNNs) are particularly well-suited for biomedical image segmentation tasks.

Among CNN-based architectures, **U-Net** has become a benchmark model for biomedical segmentation due to its ability to capture both global and local contextual information using a symmetric encoder-decoder structure.[93] However, U-Net can struggle with highly variable object morphology and low-contrast boundaries.
To improve performance in these settings, **Attention U-Net** incorporates attention gates (AGs) that learn to focus on relevant regions while suppressing irrelevant background features.[94] This is particularly useful for segmenting small or ambiguous structures such as chondrocytes and osteocytes in complex joint environments. Schlemper et al (2019), actually showed how Attention U-Net has been shown to outperform standard U-Net in segmenting datasets with overlapping or clustered structures, offering improved sensitivity and precision.[95]

Other models, such as **ResU-Net**, **V-Net**, and **nnU-Net**, offer additional enhancements like residual connections, 3D convolutions, or self-configuring pipelines, respectively.[96–98] However, Attention U-Net remains a strong choice when annotation datasets are limited and high anatomical specificity is required.

Chapter 3: Methods

3.1 Section Introduction (Objective i)

This chapter outlines the experimental methods used to investigate early-stage osteoarthritic changes in the knee joints of 6 C57BL/6 mice following total medial meniscectomy (TMM). The workflow included surgical induction of osteoarthritis, fixation and embedding of bone joint samples, and high-resolution imaging using propagation-based phase contrast X-ray microscopy (XRM). Subsequent image analysis was conducted using Dragonfly deep learning segmentation to quantify morphological features of bone and cartilage tissues. Scanning parameters were carefully optimized for sub-micron resolution imaging, and quantitative morphometric and statistical analyses were performed to assess changes in chondrocyte and osteocyte characteristics, as well as cartilage and bone thickness.

3.2 TMM Surgery and Bone Joint Sample Preparation

To model early-stage osteoarthritis (OA), a total medial meniscectomy (TMM) was performed on the right knee of male C57BL/6 mice at 8 weeks of age (n = 3 OA; n = 3 Control). OA samples were collected two weeks post-surgery, while control mice were intact. All surgical procedures were conducted in accordance with the McMaster Animal Ethics Board, ethical protocol AUP-23-24, and supervised by Dr. Jun Zhou. The TMM surgery involved transecting the medial meniscus under sterile conditions to induce localized joint destabilization. Control mice underwent sham surgery without meniscal transection.

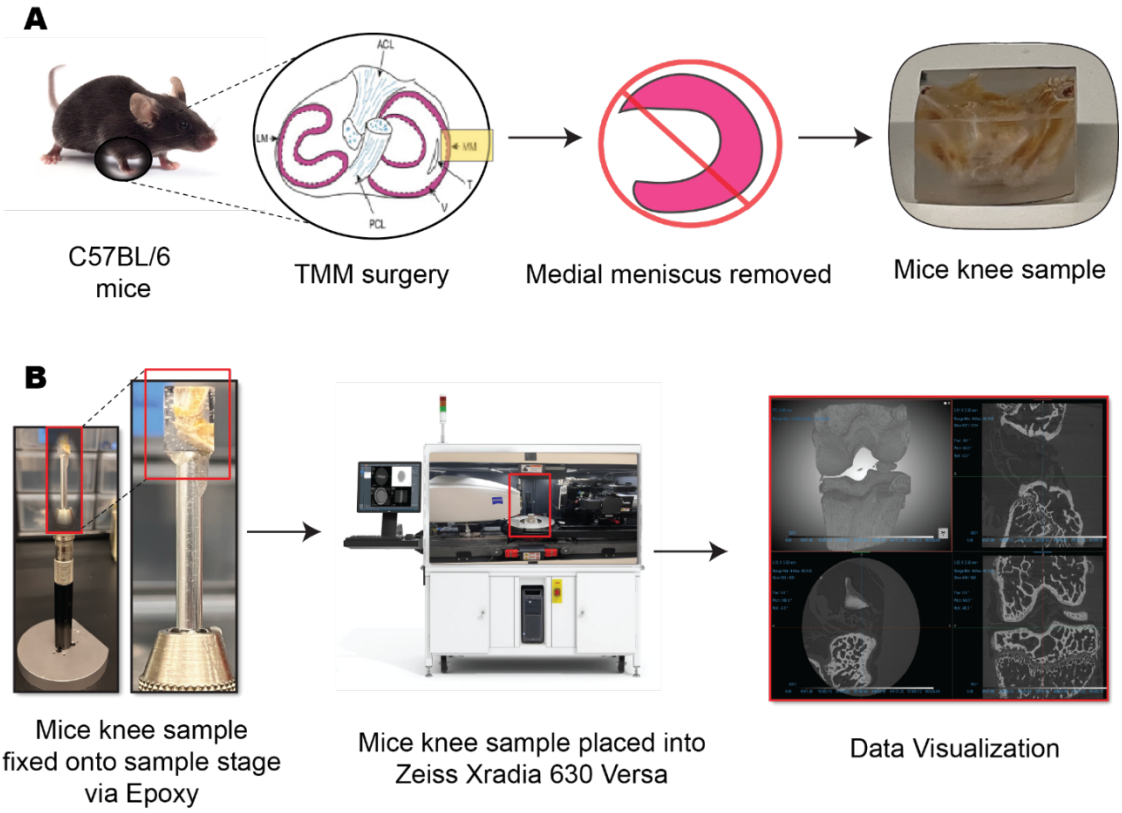

Ch. 3 – Figure 3.1. Sample preparation workflow for high-resolution imaging. *(A) Male C57BL/6 mouse knees were harvested following total medial meniscectomy (TMM). Samples were mounted on aluminum rods using epoxy. (B) Prepared joints were scanned using the Zeiss Xradia 630 Versa X-ray microscope for high-resolution imaging.*

Following surgery, the knee joint interface was harvested and fixed in 70% ethanol. Samples were then dehydrated through a graded ethanol series, beginning with 80% ethanol in deionized water for two days at room temperature with a 20-minute vacuum step to enhance infiltration. This was followed by 96% ethanol for two days and three days in 100% ethanol to ensure complete dehydration. Subsequently, samples were infiltrated with increasing concentrations of EpoFix resin in acetone (10%–100%) using incremental steps, each including a 20-minute vacuum application to promote thorough penetration. The infiltration concluded with three overnight incubations in 100% EpoFix. Finally, samples were embedded in fresh 100% EpoFix and polymerized at 60°C for 3–4 days.

3.3 Micro-CT Scanning

Samples were imaged using the Zeiss Xradia 630 Versa XRM system with the phase-contrast technique to enhance soft tissue visibility. The system utilizes a sealed lead X-ray chamber, automated stage with micron-level precision, and a Scout-and-Scan™ control

platform. Custom-cut aluminum rods were used to mount embedded samples with clear epoxy, ensuring proper alignment with the X-ray beam. The rotating stage allowed for complete 360-degree sample imaging while maintaining resolution and contrast.

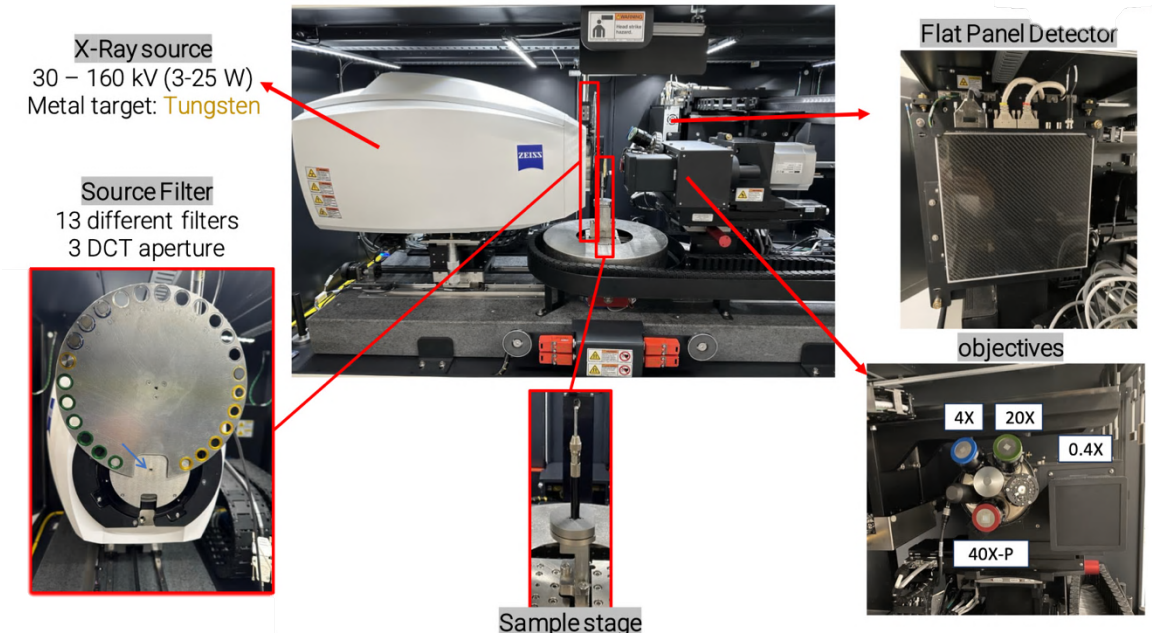

Ch. 3 – Figure 3.2. Internal components of the Zeiss Xradia 630 Versa X-ray. *Key features include the X-ray source (30–160 kV), filter wheel with 13 filter options, sample stage, flat panel detector, and a range of objectives (0.4X–40X).*

Scanning parameters were optimized based on resolution and anatomical target. The conditions for each scan type are summarized in Chapter 3.3 - Table 1 below:

Ch. 3.3 – Table 1. Conditions used for phase-contrast micro-computed tomography scanning

Resolution, µm	**8.0 (Overview)**	**1.0 (Medial)**	**1.0 (Lateral)**
Scan time, hours: minutes	2:45	6:34	5:23
Source voltage, kV	50	50	50
Source power, watts	4.5	4.5	4.5
Detector distance from sample, mm	294	264	170
Source distance from sample, mm	38.5	32	30
No. of images obtained	2001	2001	2001
Exposure time for each image, seconds	1.9	15.82	6.87
Binning	2	2	2

Following data acquisition, raw projection images were reconstructed using the Scout-and-Scan Control System. A filtered back-projection algorithm was used to generate isotropic volumetric datasets, which were then converted into 16-bit TIFF image stacks. Reconstructed images were visually inspected to verify proper alignment, contrast, and absence of motion artifacts. These datasets were subsequently imported into Dragonfly software for segmentation, 3D visualization, and quantitative morphometric analysis of bone and cartilage structures.

3.4 Image Segmentation and Analysis in ORS Dragonfly

To analyze bone and cartilage microarchitecture at the cellular level, high-resolution XRM datasets were segmented using ORS Dragonfly (Object Research Systems, Dragonfly 3D World, Zeiss Edition 2024.). The deep learning workflow began with the import of multi-slice TIFF stacks from medial and lateral scans of mouse femur–tibia joints. Files were named systematically (e.g., “0p88um-Med”) to maintain chronological integrity and allow for organized batch processing. Image stacks were loaded using the ‘Import Image’ tool, and default metadata parameters were preserved to match original acquisition settings. Once imported, stacks were rendered in a 3D interactive workspace to verify alignment and slice integrity.

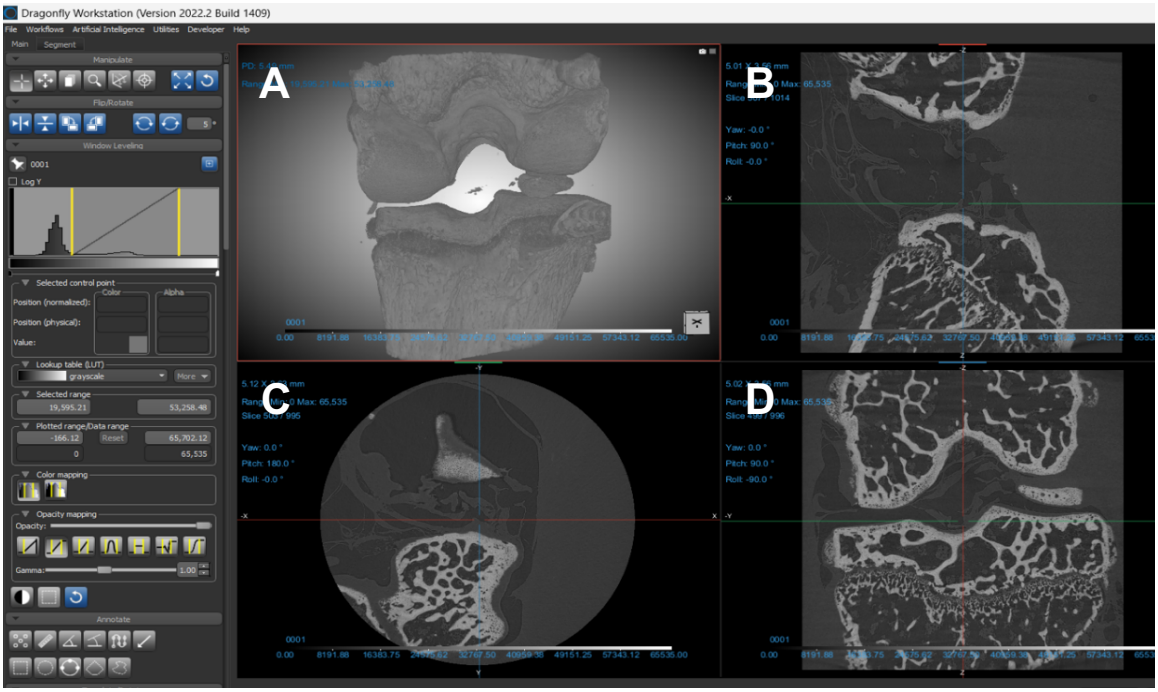

Ch. 3 – Figure 3.3. Orthogonal and 3D views of a TMM knee joint dataset in Dragonfly. *(A) 3D model reconstruction for spatial orientation prior to segmentation. (B-D) Visualization panel showing axial, sagittal, and coronal planes.*

Following import, image visualization tools such as contrast adjustment and window-leveling were applied to enhance anatomical boundaries between tissues. 3D volume rendering enabled a clear distinction between the articular cartilage (AC), calcified cartilage (CC), and subchondral bone (SCB), while orthogonal views were used to prepare for segmentation.

Annotations were created on representative slices to manually define tissue types for training a deep learning model. The articular cartilage was identified as a bright, low-density region; calcified cartilage appeared as an intermediate-density transitional layer; and subchondral bone was distinguished by its dense, hyperintense signal. Cell-level annotations were added for chondrocytes and osteocytes, using Dragonfly's object labeling and segmentation tools.

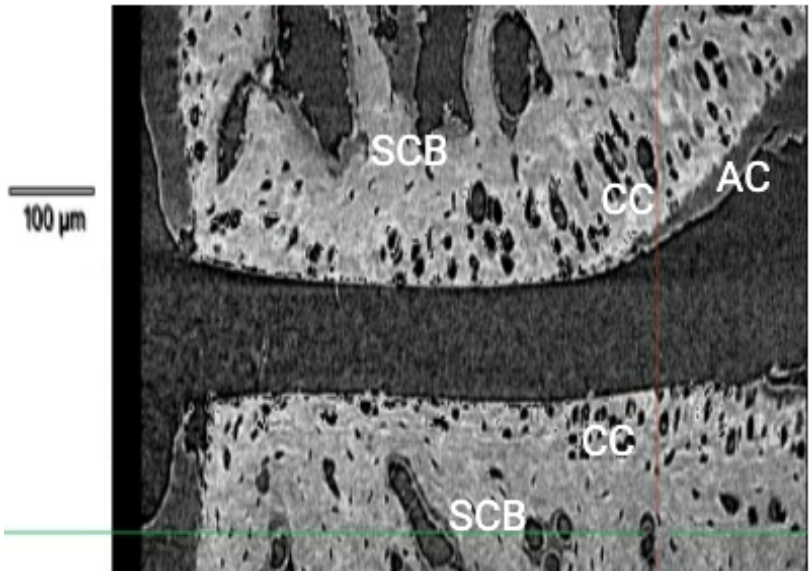

Ch. 3 – Figure 3.4. Manual annotation of tissue layers. *Orthogonal projection of a TMM knee mice model with annotations highlighting the key structures within the joint: AC, SCB, and CC.*

Manual annotations were used to train an Attention U-Net model integrated within Dragonfly's AI Segmentation Wizard. This architecture incorporates attention gates that help prioritize salient features in the training dataset, making it well-suited for complex biological images with subtle boundaries. Once trained, the model segmented the entire dataset, producing volumetric labels for AC, CC, SCB, chondrocytes, and osteocytes. The model's output was visually inspected for accuracy against the manually annotated slices.

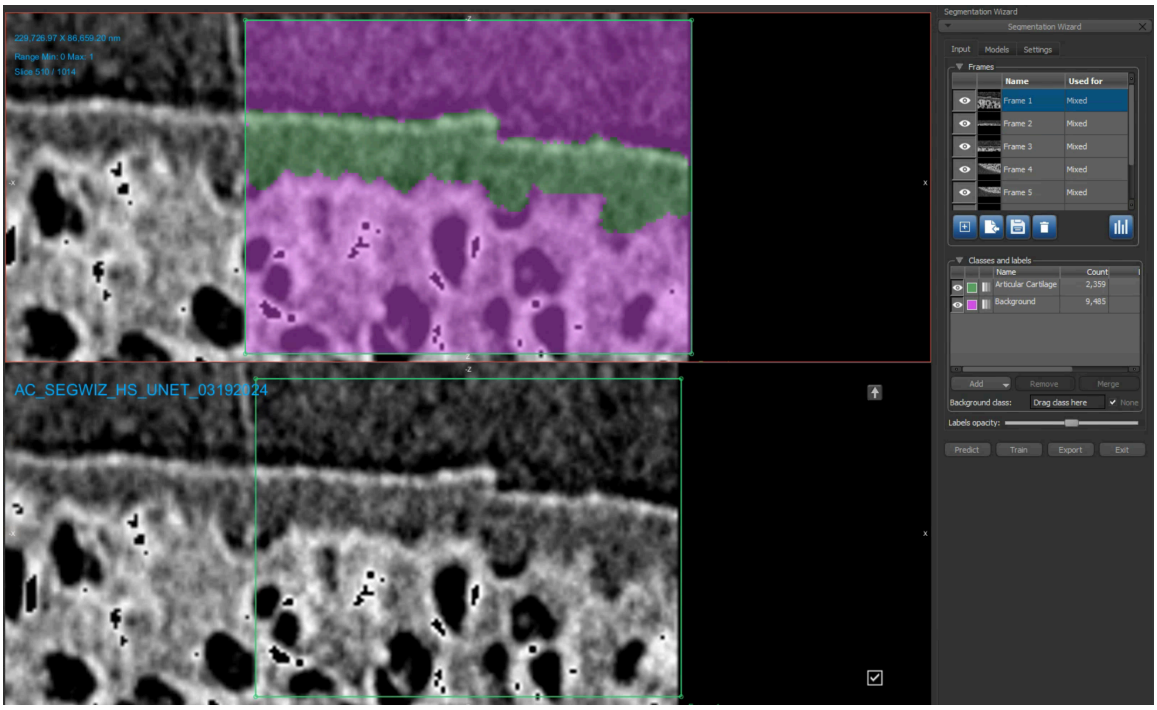

Ch. 3 – Figure 3.5. ORS Dragonfly segmentation wizard. *Green indicates the annotated articular cartilage on a single slice, while pink marks the background voxels.*

The integration of high-resolution XRM imaging with deep learning-based segmentation in Dragonfly enabled consistent and accurate identification of joint tissues and cellular features. This workflow provided the foundation for subsequent quantitative morphometric analyses, allowing for statistical comparison of structural and cellular changes between control and OA groups.

3.5 Quantitative Morphometric and Statistical Analysis

Morphometric measurements were conducted to evaluate early-stage osteoarthritis (OA) changes in bone and cartilage tissues, including cellular characteristics and compartment-specific remodeling. All analyses were performed on three control and three OA samples, comprising both femoral and tibial compartments.

3.5.1 Osteocyte Morphology and Spatial Distribution in Osteoarthritis

Quantitative analysis of osteocyte morphology and spatial distribution was performed to investigate osteoarthritis (OA)-induced changes at the cellular level. Three control and three OA samples were evaluated, each including both femur and tibia regions. Normality assumptions for all quantified variables were confirmed via the Shapiro–Wilk test. Differences in osteocyte parameters across the six subsets (femur and tibia, lateral and

medial regions, in control and OA groups) were assessed using a one-way repeated measures unbalanced ANOVA, followed by post-hoc pairwise comparisons with a Bonferroni correction. Additionally, t-tests evaluated potential significant differences in osteocyte parameters between lateral and medial regions within femur and tibia independently. Statistical significance (*) was set at $p < 0.05$ for all analyses, and very significant (**) was set at $p < 0.01$.

3.5.2 Chondrocyte Volume and Depth-Related Analysis

Quantitative analyses of chondrocyte parameters were conducted using the same statistical approach applied to osteocyte measurements. Normality of all variables was confirmed using the Shapiro–Wilk test. Differences in chondrocyte cell volume, sphericity, and depth-dependent distributions across the six anatomical subsets (femur and tibia, lateral and medial regions, in control and OA groups) were assessed using a one-way repeated measures unbalanced ANOVA, followed by Bonferroni-corrected post-hoc comparisons. Independent t-tests were used to evaluate differences between lateral and medial compartments within each bone. Statistical significance (*) was defined as $p < 0.05$.

Chondrocyte cell volume was measured to assess potential OA-related hypertrophic changes within calcified cartilage. As with osteocytes, three control and three OA samples were evaluated, each including both femoral and tibial compartments. Cell volume was measured following deep learning-based segmentation and object labeling in Dragonfly.
To investigate potential spatial reorganization of chondrocytes in response to early OA, depth-dependent distributions were analyzed across all samples. Chondrocytes were segmented and mapped relative to their vertical position within the calcified cartilage using Dragonfly's object-based measure tools. The depth from the cartilage surface was binned in intervals of 15 μm and 25 μm, and the data were normalized to allow consistent comparison across samples of varying cartilage thickness.

To evaluate potential morphological changes in chondrocyte geometry during early-stage OA, sphericity was calculated for each segmented cell. Sphericity measures how closely a cell approximates a spherical shape and is defined as the ratio of volume to surface area. Surface area in this analysis was computed using the Lindblad surface area estimator, which applies a weighted local configuration method optimized for voxel-based 3D data (Lindblad, 2005).[99]

3.5.3 Cartilage and Bone Thickness Measurements

Following segmentation of joint tissue layers, the thickness of the articular cartilage (AC) was quantitatively assessed across femoral and tibial regions in both control and OA groups. Thickness measurements were obtained using Dragonfly's *Thickness Mesh* tool, which computes local thickness values by fitting a hypothetical sphere between opposing boundary points of a segmented structure. The diameter of this sphere is recorded at each

surface point, creating a color-coded 3D mesh that represents regional thickness distribution. This approach enabled both visual inspection and quantitative extraction of localized thickness data. For each sample, thickness values were measured across the entire segmented AC volume and were then grouped by anatomical location (medial and lateral compartments of the femur and tibia). All segmentations were visually verified for boundary accuracy prior to quantification. Three control and three OA samples were analyzed, and mean values were calculated per compartment. The Shapiro–Wilk test was used to confirm data normality, and unpaired t-tests were performed to compare thickness between control and OA groups. Statistical significance was defined as $p < 0.05$.

Calcified cartilage (CC) thickness was quantified to evaluate early remodeling at the osteochondral interface. Using Dragonfly's *Thickness Mesh* tool, local thickness was measured by fitting hypothetical spheres within the segmented CC structure, producing color-coded 3D maps for visualization and analysis. Measurements were grouped by anatomical region (medial and lateral femur and tibia) and averaged across three control and three OA samples. Segmentations were visually verified, and statistical comparisons between groups were made using unpaired t-tests, with normality confirmed via the Shapiro–Wilk test ($p < 0.05$).

To evaluate whether early osteoarthritic remodeling extended to the subchondral bone plate (SCBP), thickness measurements were performed across femoral and tibial compartments in both control and OA samples. Segmentations of the SCBP were obtained following identification of the bone–calcified cartilage boundary and manually verified for consistency using grayscale overlays. Local thickness was computed using Dragonfly's Thickness Mesh tool, allowing for spatial mapping of SCB thickness and extraction of quantitative metrics across anatomical regions.

For cortical and trabecular bone analysis, all experimental data was analyzed using Prism software (GraphPad Software, California, USA). One-way or two-way analysis of variance (ANOVA) with Bonferroni correction was applied to assess statistical significance, with three samples per group (n = 3). A p-value less than 0.05 was considered statistically significant. Data are presented as the mean ± standard deviation (SD) for all graphs.

Chapter 4: Results and Discussion

4.1 Section Introduction (Objectives i, ii, iii, iv)

This chapter presents the key findings of this study, organized according to the three primary research subgoals. High-resolution phase contrast X-ray microscopy (XRM) was used to non-destructively visualize bone and cartilage tissues at sub-micron resolution, enabling detailed structural assessment throughout OA progression. To enhance visualization and quantification, all datasets were processed using deep learning-based segmentation in Dragonfly, which improved contrast, reduced background noise, and enabled accurate identification of tissue boundaries and cellular features. This segmentation workflow was essential for analyzing subtle microstructural and cellular changes across joint tissues. The results are presented across three key themes: Subgoal 1 quantifies osteocyte and chondrocyte cell volumes, including depth-dependent variations; Subgoal 2 analyzes remodeling in articular cartilage (AC), calcified cartilage (CC), and the subchondral bone plate (SCBP), with particular focus on cartilage thickness and tissue transitions; and Subgoal 3 evaluates structural changes in cortical and trabecular bone, including morphometric parameters such as bone volume fraction (BV/TV), trabecular number, cortical area, and cortical thickness. Together, these findings provide a comprehensive, high-resolution view of joint degeneration in early-stage OA.

4.2 Implementation of Phase Contrast XRM and Deep Learning-Based Segmentation (Objective I)

4.2.1. Phase Contrast XRM

Phase contrast X-ray microscopy (XRM) was implemented in this study to enhance visualization of soft tissues critical to osteoarthritis (OA) research, including the articular cartilage (AC), tendons, and ligaments. Conventional absorption-based X-ray imaging struggles to differentiate low-density structures due to minimal attenuation contrast; however, phase contrast improves visibility by detecting subtle shifts in X-ray phase as they pass through materials of varying refractive indices.[100] This is particularly important in early-stage OA, where subtle changes in cartilage thickness, surface texture, and microstructure can precede visible damage.[101,102] By increasing the source-to-detector distance (R1 + R2), this technique enhances soft tissue contrast without the need for staining or destructive sample preparation.

Figure 1 below demonstrates the impact of source-to-detector distance on image quality. Panel A, captured at 22 mm, shows limited detail within the joint, with poor definition of soft tissues. In contrast, Panel B, acquired at 110 mm, reveals enhanced contrast, clearly delineating the articular cartilage, tendon, and ligament regions. The increased distance reduces beam divergence, thereby amplifying phase effects and enabling finer separation between adjacent structures. These visual improvements directly contribute to more

accurate segmentation of tissue boundaries and make it easier to analyze and measure tissue structures later.

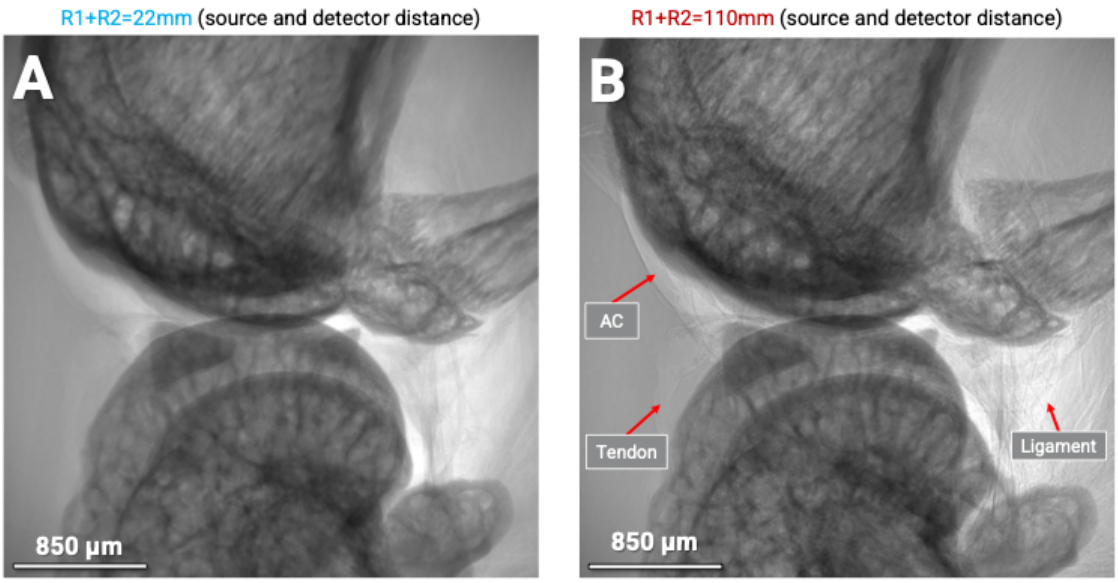

Ch. 4 – Figure 4.1. XRM Phase Contrast in Bone Samples. *A) Standard imaging at 22mm source-detector distance. B) Enhanced phase contrast imaging at 110mm distance, with clear visualization of articular cartilage, tendon, and ligament.*

Previous studies using phase contrast imaging have reported similar findings. For instance, Lee et al. (2010) demonstrated improved soft tissue differentiation using propagation-based phase contrast setups in mouse models, though their work was limited to a collagen induced mouse model as well as a conventional CT scanner.[103] More recently, Similarly, Broche et al. (2021) demonstrated the effectiveness of X-ray phase contrast imaging in revealing calcified cartilage and other joint structures in whole murine knee joints, highlighting the technique's ability to detect subtle tissue boundaries not visible with conventional imaging.[104]

Ultimately, the use of optimized phase contrast imaging in this study enabled the detailed visualization of microstructural features across the knee joint. This improvement was essential for assessing articular cartilage surface integrity, thickness, and its interface with the calcified cartilage and subchondral bone. The ability to visualize and quantify these features with clarity lays the groundwork for deeper investigation into OA onset and progression.

4.2.2. Dragonfly Deep Learning-Based Segmentation

Deep learning-based segmentation using Dragonfly software was implemented to accurately quantify morphological changes in knee joint tissues of C57BL/6 mice subjected

to TMM-induced osteoarthritis (OA). The implementation of Dragonfly's Attention U-Net deep learning model significantly enhanced the precision and accuracy in identifying and differentiating critical tissue components, including articular cartilage (AC), calcified cartilage (CC), subchondral bone (SCB), cortical bone, trabecular bone, osteocytes, and chondrocytes. Accurate segmentation facilitated precise quantitative analyses of structural and cellular changes characteristic of OA progression.

In this study, segmentation of cortical and trabecular bone regions was performed using the dual threshold method for in vivo micro-CT bone analysis, commonly referred to as the Buie method.[105] This approach was implemented using the Bone Analysis Plug-in within Dragonfly. The first threshold was applied to segment the entire bone volume, encompassing both cortical and trabecular regions, and was determined using Otsu's method to differentiate bone from non-bone areas. The second threshold enabled the separation of cortical and trabecular compartments by identifying differences in grayscale intensity values. These thresholds were optimized through visual inspection by multiple users to ensure accurate segmentation across all specimens. A representative 3D visualization of segmented femoral cortical and trabecular bone is shown in Figure 2, processed using the Bone Analysis Plug-in.

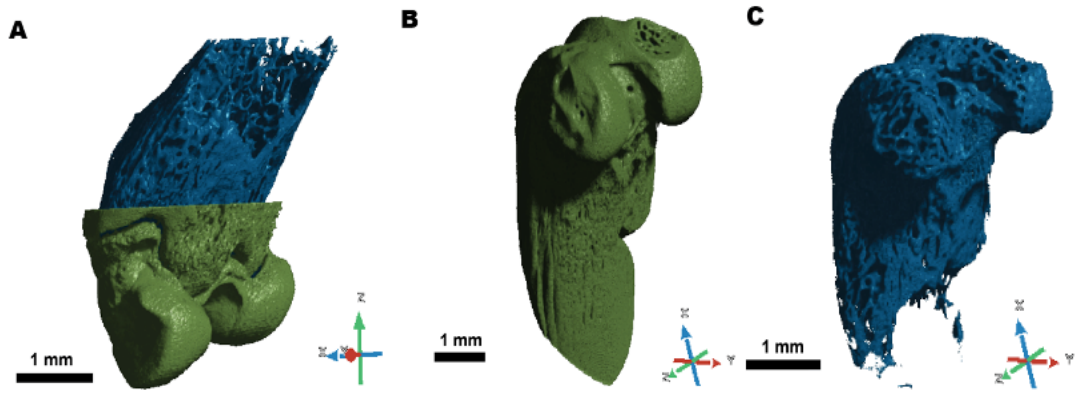

Ch. 4 – Figure 4.2. 3D rendering of the femur bone showing cortical (green) and trabecular (blue) bone regions*. Panel A provides an overview of the entire femur with clipping done to illustrate both regions. Panel B zooms in with a clipped view to highlight the cortical bone. Panel C shows a different angle of the trabecular bone, emphasizing its internal structure.*

After segmenting the femur and cortical bone using the Dragonfly deep learning framework, the process was extended to isolate articular cartilage for assessing OA-induced changes. This segmentation incorporated the Dragonfly snap grid feature along with Otsu thresholding to accurately distinguish between bone and articular cartilage. As shown in Figure 3 (Panel B), the resulting clear delineation of articular cartilage boundaries was confirmed by thorough visual inspection, establishing a reliable basis for subsequent quantitative analyses, such as measurements of cartilage thickness, surface area, and volume.

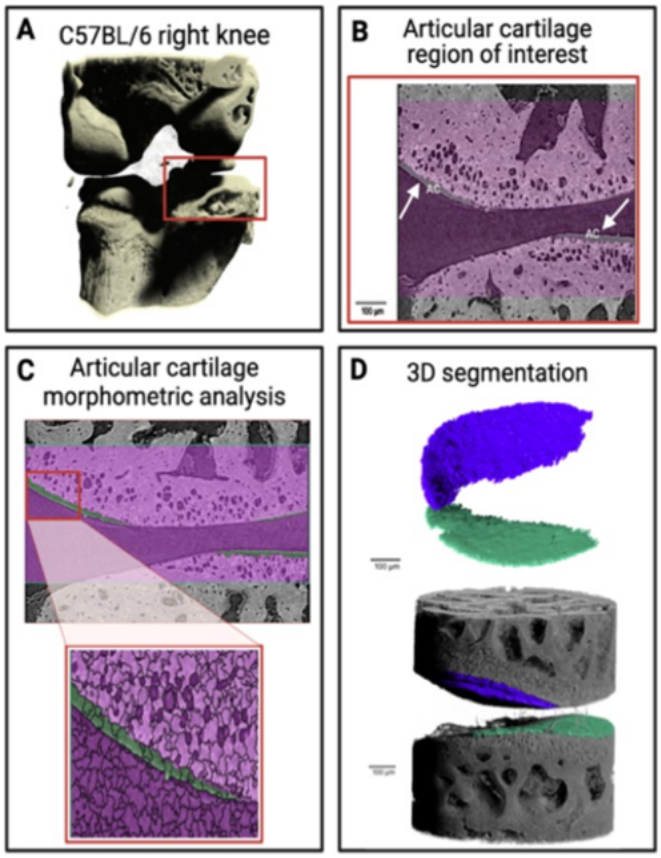

Ch. 4 – Figure 4.3. Multi-stage visualization and segmentation of articular cartilage in the medial tibial plateau of a C57BL/6 mouse knee following TMM-induced osteoarthritis. *(A) 3D rendering of the right knee joint with region of interest highlighted in red. (B) High-resolution slice showing articular cartilage (AC, white arrows). (C) 64x64 snap grid feature detection within dragonfly for articular cartilage segmentation. (D) 3D segmentation of femur articular cartilage (blue) and tibial articular cartilage (green)*

In addition to distinguishing major tissue types, the segmentation approach enabled detailed characterization of cellular components. Within figure 4, high-resolution grayscale imaging allowed clear differentiation of tissue boundaries, while the corresponding segmentation maps identified and delineated chondrocytes (yellow), osteocytes (blue), articular cartilage (green), calcified cartilage (pink), and bone tissue (orange). This integrated imaging strategy lays the foundation for comprehensive quantitative analyses of both tissue architecture and cellular organization.

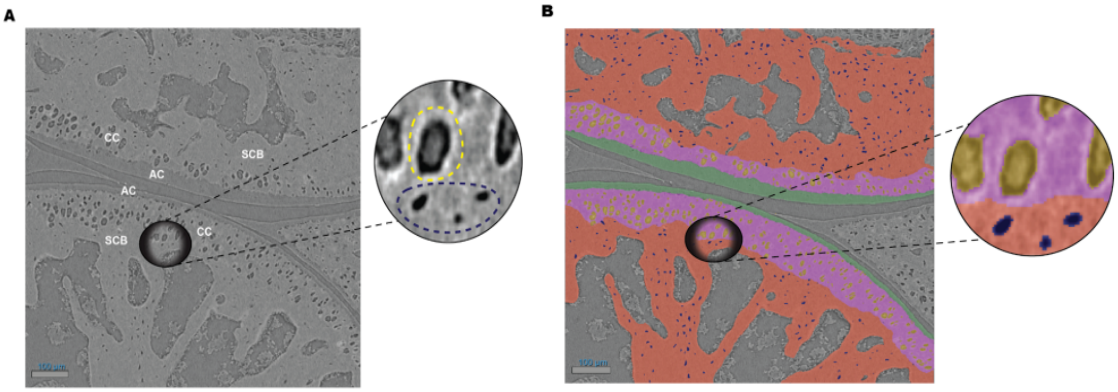

Ch. 4 – Figure 4.4. Grayscale imaging and segmentation of bone components. *Panel A displays a 2D grayscale image of the bone sample with zoomed-in regions marked by dashed lines, where the yellow dashed outline highlights a chondrocyte, and the blue dashed outline denotes an osteocyte. Panel B shows the corresponding segmentation model overlaid on the image, with chondrocytes in yellow, osteocytes in blue, articular cartilage in green, calcified cartilage in pink, and bone components in orange.*

Finally, further analysis focused on cellular distributions within joint tissues to enhance understanding of OA at a microstructural level. High-resolution imaging revealed distinct spatial distributions of osteocytes and chondrocytes, with segmentation techniques clearly delineating individual cell boundaries. To further improve accuracy, distance mapping combined with watershed transformations was applied, ensuring that each osteocyte lacuna and chondrocyte was uniquely identified and counted as a single unit. This refined approach enabled reliable quantitative measurements of cellular localization and density, laying a foundation for subsequent detailed analyses of joint tissue morphology.

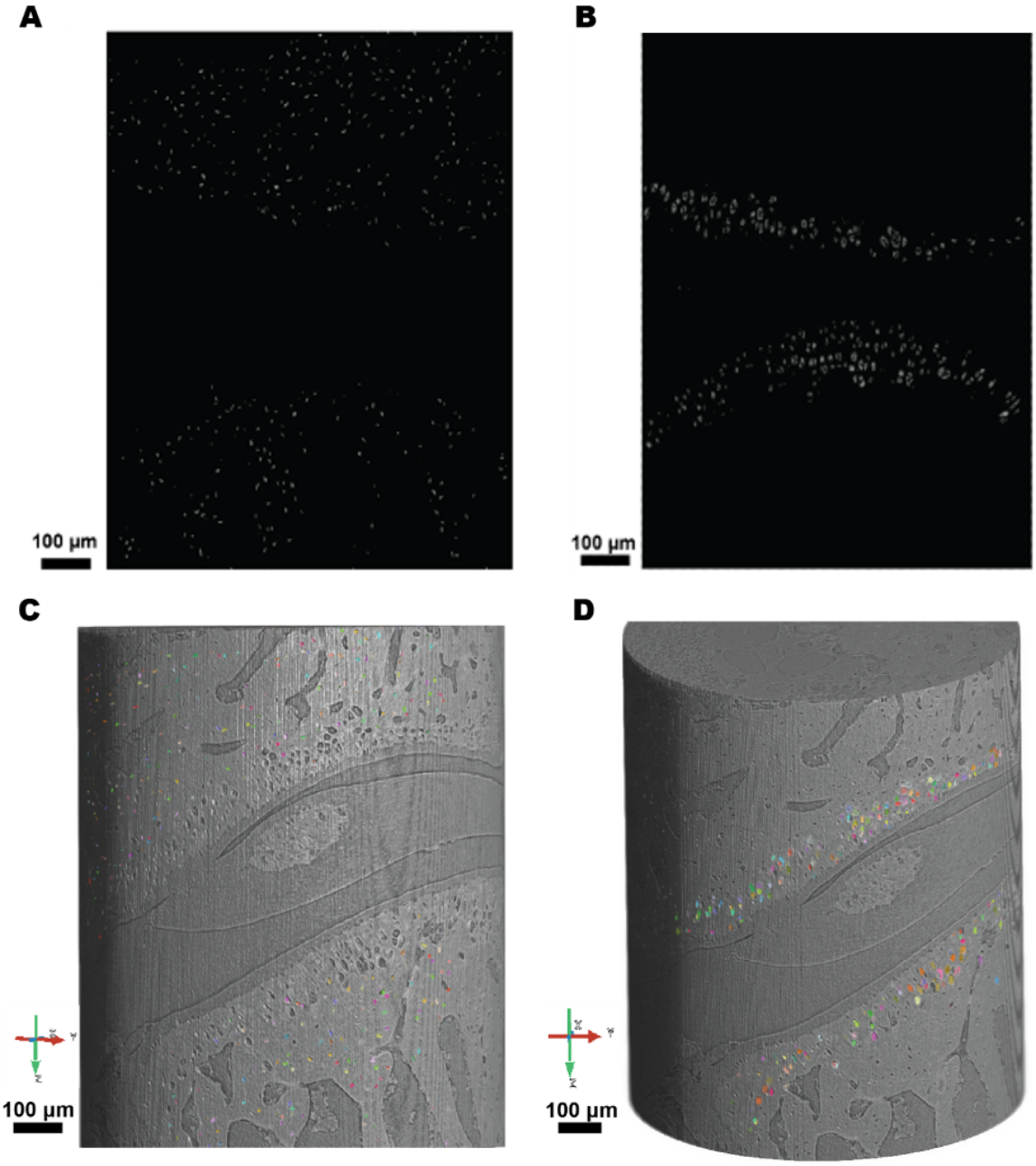

Ch. 4 – Figure 4.5. Enhanced cellular segmentation using distance mapping and watershed transformation. *Panels (A) and (B) depict the distance maps for osteocytes and chondrocytes, respectively, which facilitate watershed transformation and ensure that each cell is labeled as a distinct class. Panel (C) shows the color-coded segmentation of osteocytes, with each hue representing an individual cell for accurate measurements. In Panel (D), chondrocyte segmentation is overlaid in color onto a mice knee joint 3D model, highlighting the spatial distribution of chondrocytes.*

In recent years, deep learning has become an interesting area within osteoarthritis research for its ability to automate and refine tissue segmentation. For example, Zhang et al. (2018) demonstrated that convolutional neural networks significantly enhanced cartilage segmentation accuracy from MRI data, while Kumar et al. (2019) showed that deep learning outperformed traditional thresholding techniques in detecting OA-related structural changes.[106,107] In the present work, Dragonfly's Attention U-Net model was used to achieve precise delineation of tissue interfaces, including articular cartilage, calcified cartilage, and bone, and was further augmented with distance mapping and watershed transformations for detailed cellular segmentation. This approach not only provided quantification of both macrostructural and microstructural changes which will be discussed in the next section but also confirmed the potential of deep learning techniques to provide measurements for OA assessments.

4.3 Quantification of Osteocyte and Chondrocyte Cell Volumes and Depth-Dependent Changes (Objective IV)

4.3.1. Osteocyte Cell Volume Comparison

Quantitative analysis of osteocyte cell volumes revealed morphological differences between OA and control groups. Figure 1A demonstrates a statistically significant decrease ($p < 0.01$) in osteocyte volume specifically in OA sample 1 compared to its corresponding control, while samples 2 and 3 showed no significant differences. When further examining osteocyte volumes across anatomical sites (femur versus tibia) and specific regions (lateral versus medial), no statistically significant differences were found (Figure 1B). This suggests that OA-induced changes in osteocyte morphology occur uniformly across bone compartments rather than being localized to specific regions.

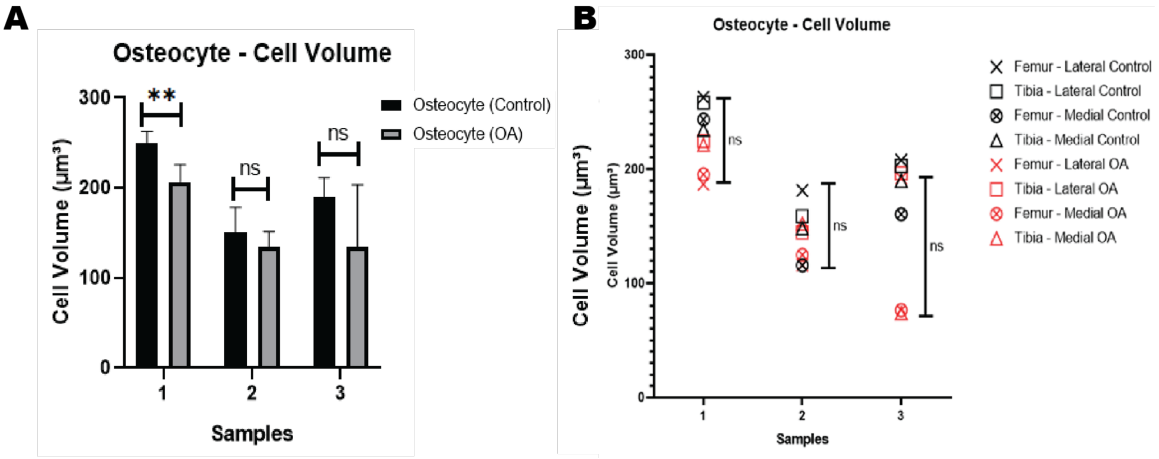

Ch. 4 – Figure 4.6. Osteocyte cell volume comparisons in control vs OA. *(A) Mean osteocyte cell volume (µm³) in control and OA groups demonstrating significant reductions in OA (**, $p < 0.01$). (B) Comparative osteocyte cell volumes across femur and tibia lateral and medial regions for control and OA, showing no significant region-specific differences. ns = not significant.*

These findings partially support the original hypothesis, which anticipated detectable cellular volume changes via high-resolution X-ray microscopy (XRM) combined with deep learning-based segmentation. Contrary to expectations of increased osteocyte cell volumes indicative of hypertrophy during early OA stages, this analysis instead indicated a decrease in cell volume in one OA sample, and no clear volume increase in the remaining samples. The limited significance and inconsistent trends across samples suggest variability in individual responses to OA at the early stages investigated. Such variability aligns with Kim et al. (2013), reporting heterogeneity in early-stage OA responses in C57BL/6 mice, where microstructural and cellular changes may not yet exhibit consistent or pronounced alterations.[108]

The observed decrease in osteocyte volume in OA samples may reflect early-stage cellular adaptation or stress-induced morphological remodeling rather than the initially hypothesized hypertrophy. This interpretation aligns closely with previous findings by Tiede-Lewis et al. (2017), who reported significant age-related reductions in osteocyte cell body volume (approximately 19%) in male mice, accompanied by corresponding decreases in lacunar volume.[109] Such findings suggest that osteocyte cell and lacunar volume reductions can occur as part of an early or adaptive response to altered mechanical or biological stress. Similarly, the variability and limited significant changes observed in this study's osteocyte volumes emphasize the complex nature of cellular responses during early OA progression. Collectively, these data highlight the sensitivity of XRM in capturing subtle morphological variations in osteocytes and underscore the necessity of carefully considering individual and sample-specific differences when analyzing early OA-related changes.

Osteocyte Lacunae Characteristics

Further characterization of osteocyte lacunae included total lacunal volume, lacunar density, and depth-dependent distribution within bone regions. In comparing total lacunal volume and lacunal density (Figure 2A and 2B), no significant differences emerged between control and OA groups. However, depth-dependent analyses (Figures 2C and 2D) provided deeper insights, showing a shift in osteocyte distribution in OA samples toward superficial (subchondral) regions of bone (bins 100–150 μm depth range). This altered cellular distribution pattern could reflect an adaptive or degenerative response associated with cartilage deterioration and mechanical stress redistribution in OA.

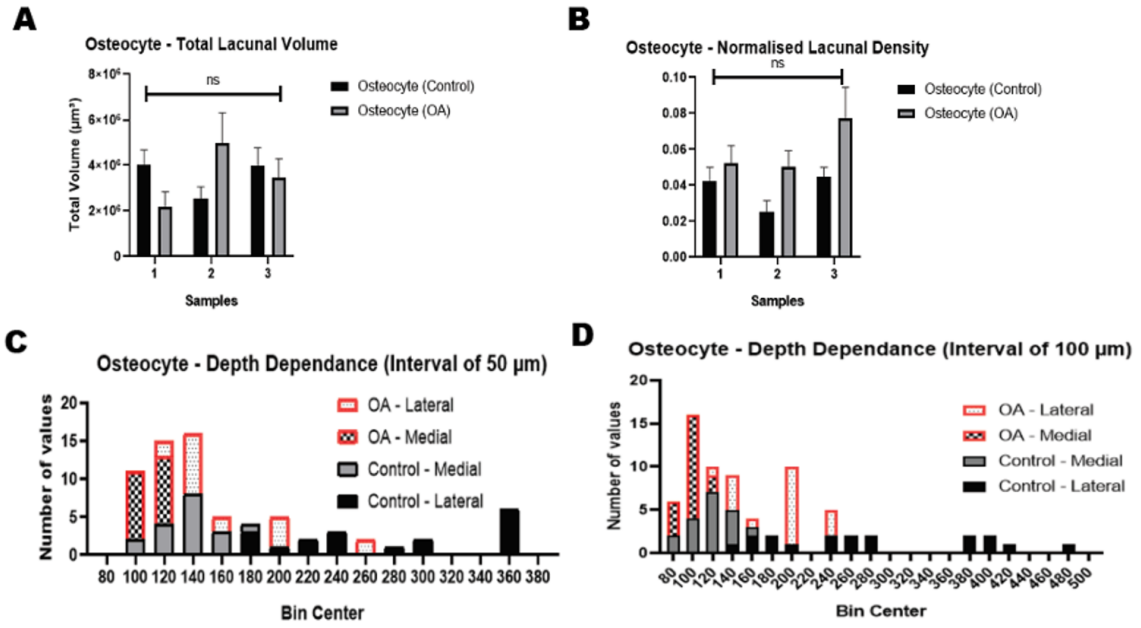

Ch. 4 – Figure 4.7. Osteocyte lacunae characteristics and depth dependence. *(A-B) Total lacunal volume and normalized lacunal density between OA and control groups (ns = not significant). (C-D) Depth-dependent osteocyte distribution demonstrating OA-induced shifts towards superficial bone regions.*

Although significant changes in total lacunal volume or density were not observed, the clear shift of osteocytes toward superficial subchondral regions supports the hypothesis of detectable early-stage adaptive responses. This redistribution may represent an initial compensatory mechanism, reflecting altered local mechanical conditions and stress gradients typically associated with early-stage OA.[110]

Literature supports the notion of spatial cellular shifts in OA progression. For example, Burr and Gallant (2012) described changes in osteocyte localization and density as indicative of bone remodeling due to altered mechanical loading conditions in OA.[30] Similarly, Palacio-Mancheno et al. (2014) demonstrated that osteocyte lacunar architecture is sensitive to mechanical loading conditions, with spatial redistribution and alignment changes reflecting bone adaptation. These findings support the notion that altered mechanics, such as those occurring in early OA, may drive similar adaptive osteocyte responses.[111] The depth-dependent shifts noted in the present study further reinforce the potential role of osteocyte spatial organization as an early and sensitive indicator of OA-related bone adaptation. The absence of significant lacunal volume or density changes in early OA suggests that morphological alterations at this stage may primarily involve cell redistribution rather than pronounced structural remodeling. Overall, these results emphasize the sensitivity of XRM-based segmentation techniques in capturing subtle yet significant early OA-induced microstructural changes and highlight the importance of carefully interpreting these depth-dependent cellular redistributions as early indicators of disease adaptation.

Regional Comparisons and Cellular Shape Analysis

Regional comparisons of osteocyte morphology were performed to assess whether OA-related changes varied by anatomical location across the femur and tibia. As shown in Figure 3, total lacunar number and osteocyte sphericity were analyzed across lateral and medial regions in both control and OA groups. No statistically significant differences were found among any of the anatomical subgroups.

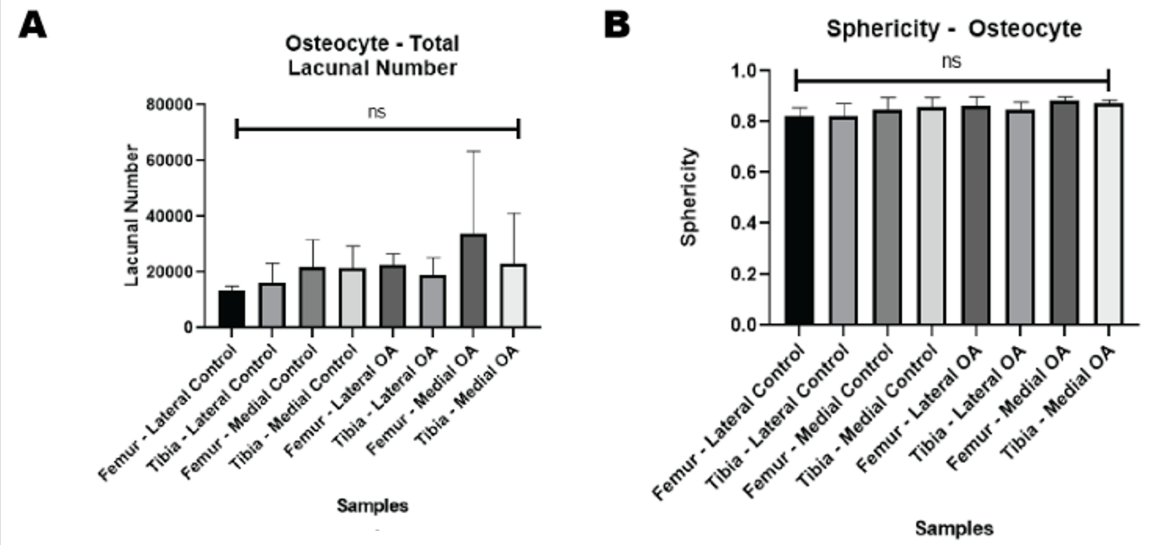

Ch. 4 – Figure 4.8. Osteocyte lacunar number and sphericity across anatomical regions. *(A) Total lacunar number segmented and labeled post-watershed (ns = not significant). (B) Osteocyte sphericity calculated as the ratio of volume to surface are.*

The total lacunal number, derived from Dragonfly's object labeling following watershed transformation, showed variability across samples but no consistent trend or statistical significance. This suggests that OA does not substantially alter the overall number of osteocyte lacunae across femoral and tibial compartments in early OA stages. The absence of significant differences in total osteocyte lacunar number between control and OA groups in this study aligns with findings from previous research. For instance, Carpentier et al. (2012) reported that, while the proportion of hypermineralized osteocyte lacunae increased in osteoarthritic bone, the total lacunar number density did not differ significantly between osteoarthritic and control samples.[112] This study along with the results shown suggest that early-stage OA may not drastically affect the overall number of osteocyte lacunae. Similarly, Murtavoic et al. (2023), reported on subchondral bone in OA patients and found no significant change in osteocyte lacunar density between moderate and severe OA stages, indicating that lacunar density remains relatively stable during early OA progression.[113] These consistent observations imply that, in the initial phases of OA, osteocyte lacunar density may be preserved, with alterations potentially occurring in other aspects of bone microarchitecture or at later disease stages.

Similarly, osteocyte sphericity, calculated as the ratio of cell volume to surface area, showed no significant changes across all sample groups. This parameter reflects how closely each osteocyte approximates a spherical shape. In this case, surface area was calculated using the Lindblad surface area estimator, which applies a weighted local configuration method for 3D voxel data.[99] The stability of sphericity across regions and conditions in this study suggests that early-stage OA does not substantially alter osteocyte geometry. These findings are consistent with observations by Hemmatian et al. (2017), who reported that while osteocyte lacunar morphology influences local bone tissue strains, significant changes in lacunar shape, such as increases in sphericity, were more commonly associated with advanced age or later stages of OA degeneration.[64] In earlier stages, such as those investigated in this study, osteocyte shape remained relatively stable. This supports the interpretation that geometric remodeling of osteocytes may be a later event in OA progression, whereas early changes are more likely to manifest in spatial redistribution or cell volume rather than shape. Together, these results demonstrate the ability of high-resolution imaging for detecting early-stage cellular responses and reinforce the need to consider disease timing when evaluating osteocyte morphology.

4.3.2. Chondrocyte Cell Volume Analysis

Chondrocyte cell volumes was measured to assess potential OA-related hypertrophic changes within calcified cartilage. As with osteocytes, three control and three OA samples were evaluated, each including both femoral and tibial compartments. Cell volume was measured following deep learning-based segmentation and object labeling in Dragonfly.

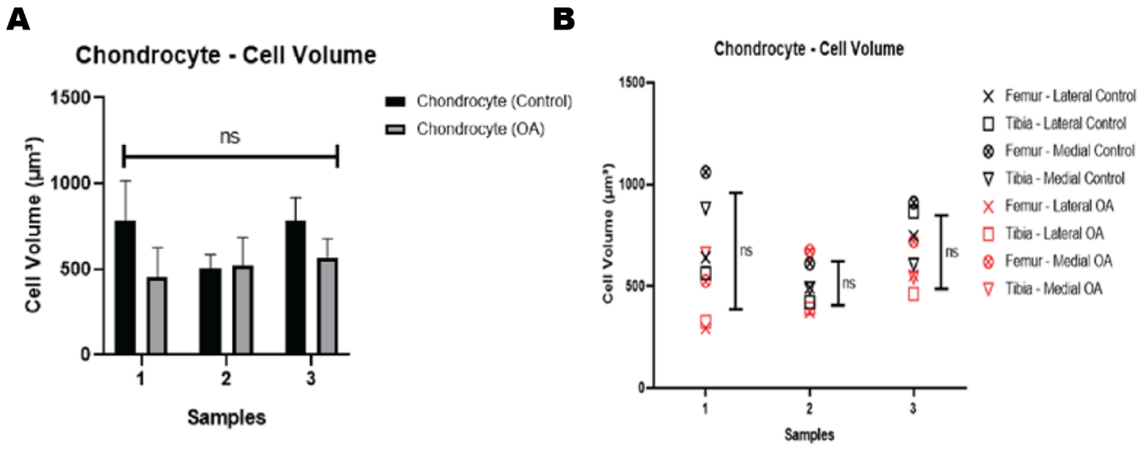

Ch. 4 – Figure 4.9. Chondrocyte cell volume comparisons in control vs OA. *(A) Mean osteocyte cell volume (µm³) in control and OA. (B) Comparative osteocyte cell volumes across femur and tibia lateral and medial regions for control and OA. ns = not significant*

As shown in Figure 4A, chondrocyte volumes in OA samples were consistently lower than their respective controls across all three sample groups; however, none of these differences

reached statistical significance. When further stratified by anatomical site, femur versus tibia, and lateral versus medial compartments **(**Figure 4B**),** no regional differences were observed, and the overall distribution of chondrocyte volumes remained consistent between OA and control conditions. These findings do not support the original hypothesis, which anticipated an increase in chondrocyte volume as a marker of early hypertrophy driven by OA progression. Instead, the lack of statistically significant differences suggests that, at the early time point assessed in this study, chondrocyte hypertrophy may not yet be morphologically apparent.

Notably, prior studies have documented chondrocyte hypertrophy in early OA models, particularly within the calcified cartilage layer, where hypertrophic differentiation is considered a hallmark of disease progression.[36] In early osteoarthritis (OA), chondrocyte hypertrophy is often regionally confined and temporally variable. For instance, Kamekura et al. (2005) observed that type X collagen and MMP-13 were markedly induced and colocalized in the early-stage OA cartilage of murine models, particularly in the superficial and middle zones above the tidemark. However, these molecular changes occurred without consistent alterations in overall chondrocyte cell size.[114,115] This suggests that molecular alterations may precede measurable volumetric expansion during the early transitional phase of OA progression.

Depth-Dependent Chondrocyte Distribution

To evaluate spatial changes in chondrocyte organization during early OA, depth-dependent distributions were analyzed across all samples. Chondrocyte positions were quantified relative to the cartilage surface to assess shifts in localization across zones.

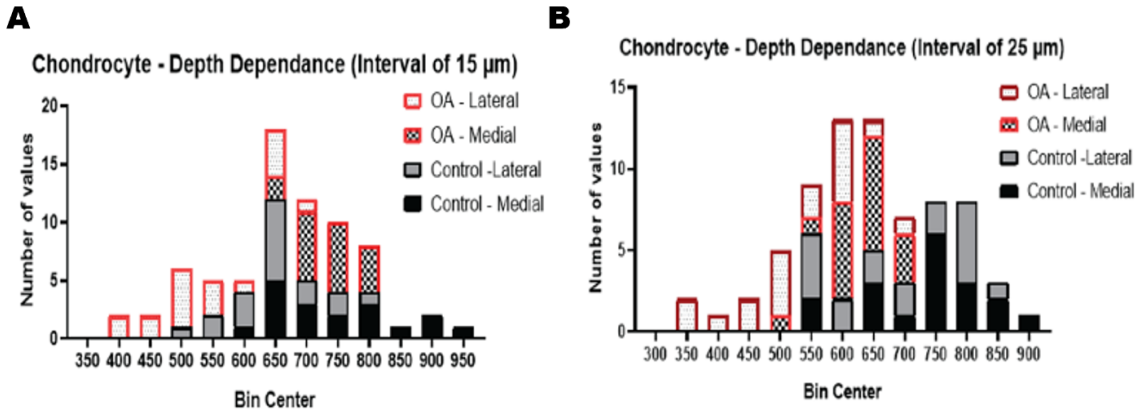

Ch. 4 – Figure 4.10. Depth-dependent chondrocyte distribution in calcified cartilage. *(A–B) Normalized chondrocyte frequency plotted at 15 µm and 25 µm depth intervals from the cartilage surface.*

In control samples, chondrocytes exhibited a relatively uniform distribution throughout the cartilage depth, with a higher density toward the mid to deeper zones. In contrast, OA

samples showed a distinct shift, with increased chondrocyte density concentrated in the superficial to mid-depth regions. This superficial redistribution may reflect early structural changes and altered load-bearing conditions in cartilage undergoing degeneration. Notably, this pattern was consistent across both femoral and tibial compartments. This shift in chondrocyte localization aligns with previous studies describing altered zonal organization in cartilage affected by OA. In particular, Tschaikowsky et al. (2022), demonstrated that early OA is characterized by progressive reorganization of superficial chondrocyte patterns, from linear strings to double strings and eventually to small clusters, highlighting a disruption of normal cellular architecture in the upper cartilage zones.[116]

The depth-dependent analysis in this study supports the hypothesis that early-stage OA induces subtle, yet detectable, changes in cartilage organization at the cellular level. These alterations may serve as early changes of tissue adaptation or degeneration, which precede measurable structural loss or chondrocyte hypertrophy. Together, these findings highlight the ability of XRM imaging and segmentation techniques in capturing early cellular responses to joint degeneration.

Chondrocyte Sphericity and Shape Preservation

To determine whether early OA alters chondrocyte geometry, sphericity was calculated for all segmented cells across anatomical regions. This analysis assessed potential shape changes independent of volume or spatial distribution.

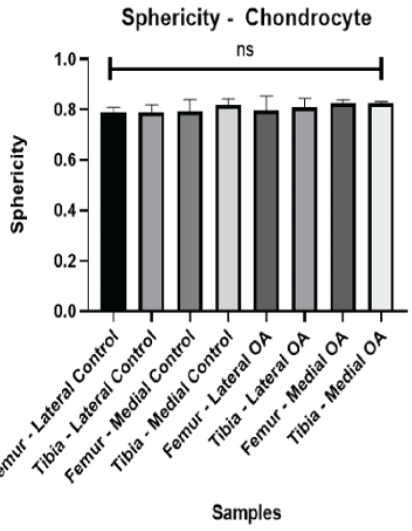

Ch. 4 – Figure 4.11. Chondrocyte sphericity in control and OA groups. *Quantification of chondrocyte sphericity across femur and tibia, lateral and medial regions. ns = not significant.*

As shown in Figure 6, no statistically significant differences in chondrocyte sphericity were observed between control and OA groups across femoral or tibial regions. Chondrocyte shapes remained largely uniform, with no apparent shift toward more

elongated or irregular geometries in early-stage OA samples. This result suggests that despite early changes in chondrocyte localization, overall cell shape remains preserved at this stage of disease progression. These findings align with the observations of Rim et al. (2020), who noted that chondrocyte hypertrophy and senescence are more prominent in later stages of OA and are associated with cartilage breakdown and matrix remodeling. However, the study also highlighted that the sequence of these events, whether hypertrophy or senescence initiates the degenerative cascade, remains unclear.[117] In this study, the stable chondrocyte shape likely reflects an early stage of disease, where changes may be starting at the molecular or spatial level but have not yet affected cell morphology. This supports the interpretation that chondrocyte shape alterations may emerge only in more advanced phases of OA, while early-stage responses may be confined to spatial reorganization or molecular shifts.

4.4 Remodeling of Articular Cartilage, Calcified Cartilage, and Subchondral Bone Plate (Objective III)

4.4.1. Delineation and Segmentation of Joint Tissue Interfaces

Accurate segmentation of the articular cartilage (AC), calcified cartilage (CC), and subchondral bone plate (SCBP) was imperative for analyzing tissue-level changes associated with early-stage OA. In this study, segmentation was performed using a manual visual delineation process, guided by distinct grayscale contrast differences in phase-contrast XRM images. These anatomical boundaries were identified based on their relative position and grayscale intensity, consistent with established tissue organization in the mouse knee joint.

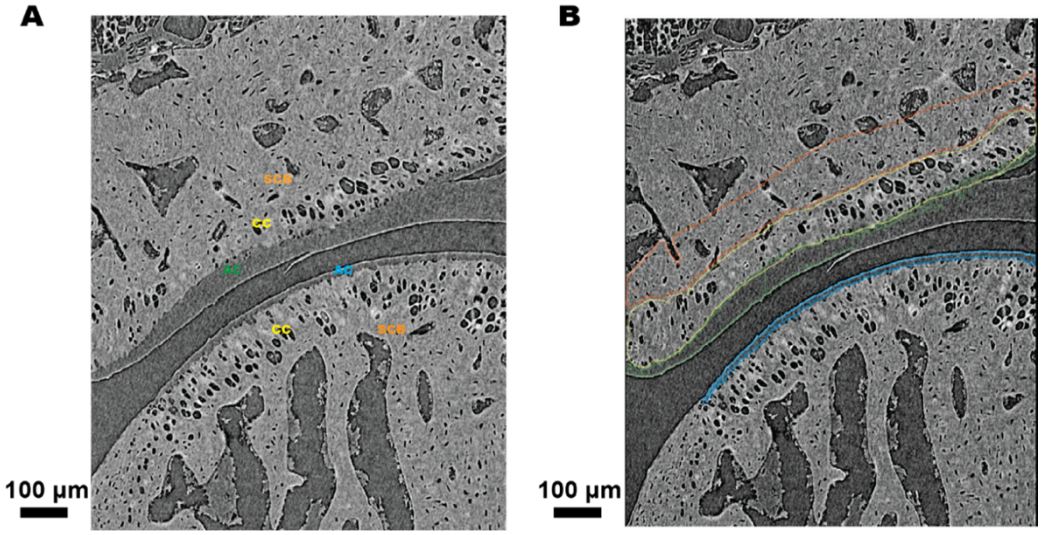

Ch. 4 – Figure 4.12. Visual segmentation of AC, CC, and SCB. *(A) Grayscale XRM image labeled to show articular cartilage (AC), calcified cartilage (CC), and subchondral bone plate (SCB) regions. (B) Overlay of traced boundaries used during segmentation to delineate the interfaces between tissue compartments.*

The articular cartilage was characterized by its superficial location, smooth contour, and uniform low-density signal. Directly beneath the AC, the calcified cartilage appeared as a denser band with an abrupt grayscale transition, indicating mineralization. This interface, known as the tidemark, was used to distinguish the AC-CC boundary. Finally, the subchondral bone plate was defined by its higher grayscale intensity and trabecular continuity beneath the CC layer.

4.4.2. Articular Cartilage Thickness Changes in Early OA

Following segmentation of joint tissue layers, the thickness of the articular cartilage (AC) was quantitatively assessed across femoral and tibial regions in both control and OA groups.

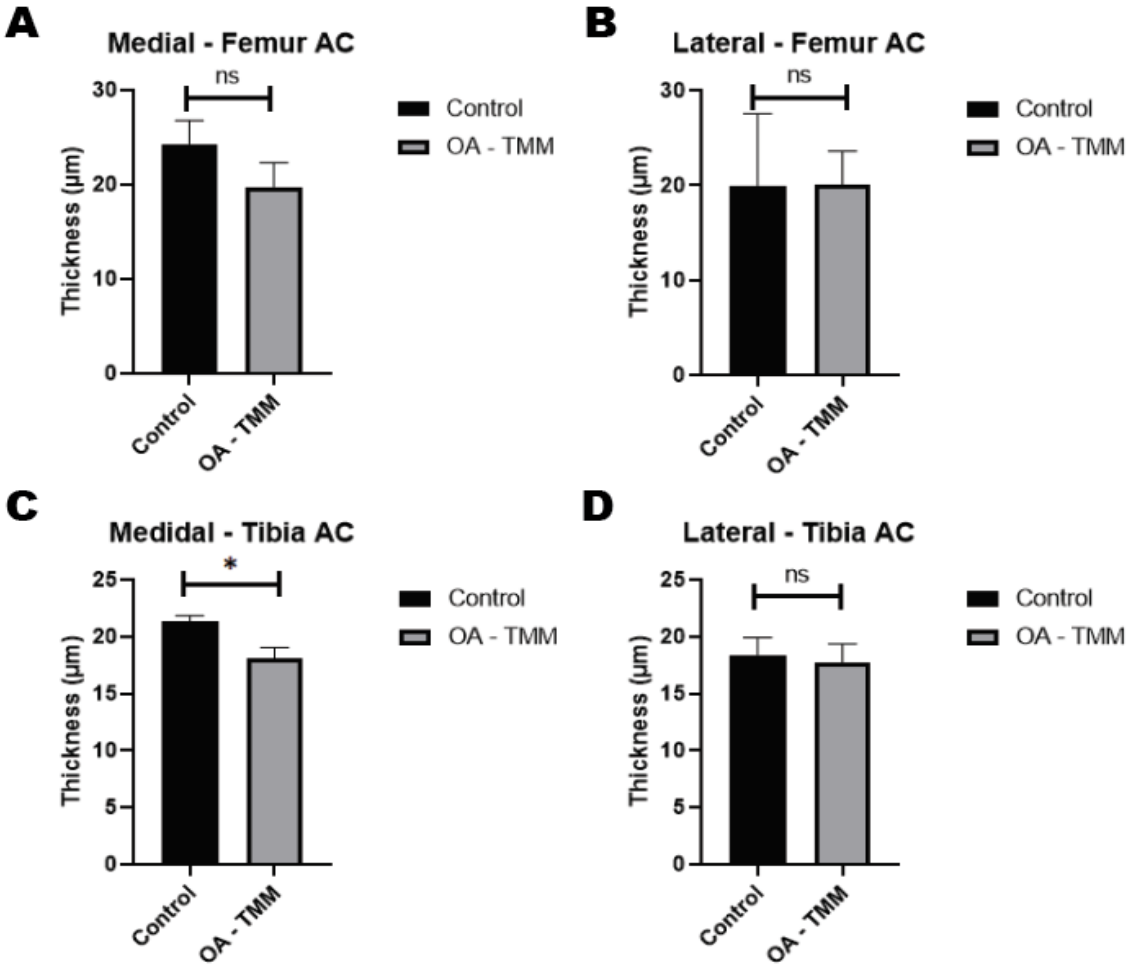

Ch. 4 – Figure 4.13. Articular cartilage thickness measurements across compartments. *(A–D) Thickness of articular cartilage (AC) in femur and tibia, medial and lateral compartments. (C), $p < 0.05$. ns = not significant.*

As shown in Figure 2, bar plots compare AC thickness across all anatomical regions. A statistically significant reduction in AC thickness was observed in the medial tibial compartment of OA samples compared to controls (Figure 2C, $p < 0.05$). No other regions, including the medial femur, lateral femur, or lateral tibia, demonstrated significant differences (Figures 2A, 2B, 2D; *ns* = not significant). This localized thinning suggests that the tibial cartilage is more susceptible to early degeneration following TMM-induced OA, particularly in the medial region where mechanical loading is concentrated.

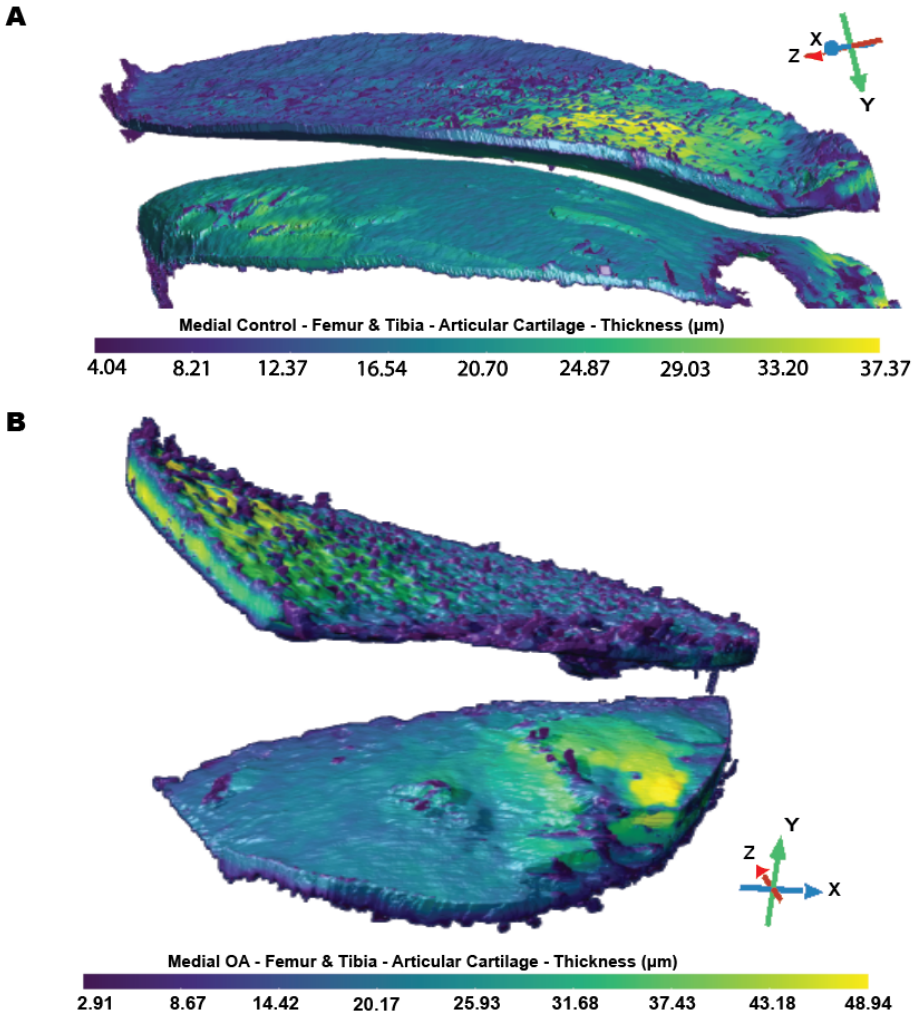

Ch. 4 – Figure 4.14. 3D visualization of femoral medial articular cartilage thickness. *(A) Control sample shows continuous cartilage surface. (B) OA sample shows regions of surface thinning. Thickness is colour coded according to the scale bar, where purple indicates lower thickness values and yellow represents greater thickness.*

To visualize these microstructural changes in 3D, segmented AC surfaces were rendered for representative medial femur regions in control and OA samples (Figure 3). In Panel A, the control sample demonstrates a relatively uniform and continuous cartilage surface. In

contrast, Panel B shows the OA sample, where localized thinning and surface roughness are evident.

The observed pattern of articular cartilage thinning observed in this study, specifically the significant reduction in the medial tibia, with no changes in the femur, likely reflects mechanical loading differences inherent to the TMM-induced OA model. Tibial cartilage, particularly on the medial side, experiences increased compressive stress following meniscal destabilization, making it more susceptible to early degeneration.[118] Glasson et al. (2007), have shown that the tibial plateau bears a disproportionate share of joint loading in rodent models of OA, especially following surgical destabilization.[15] However, it is important to note that this finding is not universally consistent across all OA studies. For example, Hada et al. (2014), have reported greater degeneration in femoral cartilage compared to tibial regions during early stages of human knee OA.[119] These discrepancies may reflect species-specific biomechanical differences, the influence of loading models, or variation in OA stage and disease progression. Thus, the localized cartilage loss observed in the medial tibia of this TMM-model may represent an early and model-specific manifestation of OA-related remodeling.

4.4.3. Visualization and Quantification of Calcified Cartilage Remodeling

Calcified cartilage (CC) thickness was quantified to evaluate early remodeling at the osteochondral interface.

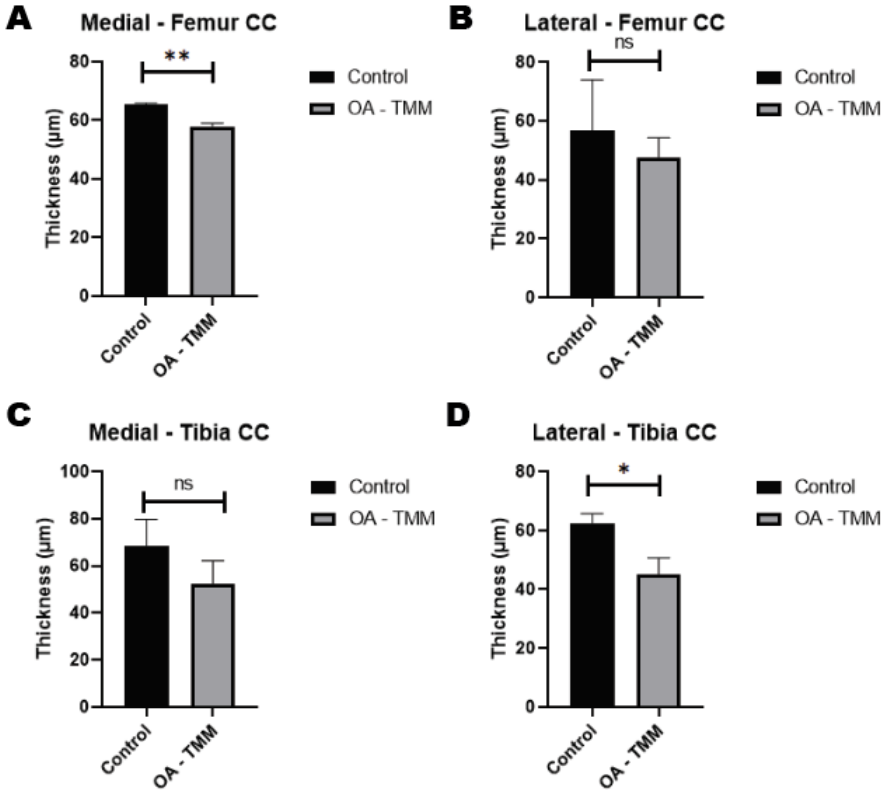

Ch. 4 – Figure 4.15. Calcified cartilage thickness measurements across compartments. *(A–D) Thickness of calcified cartilage (CC) in medial and lateral femur and tibia regions. Statistically significant reductions are shown in the medial femur (A) and lateral tibia (D). $p < 0.05$. ns = not significant.*

As shown in Figure 4, significant reductions in calcified cartilage thickness were observed in the medial femur and lateral tibial compartments of OA samples compared to controls (Figures 4A and 4D). No significant changes were detected in the medial tibia or lateral femur (Figures 4B and 4C).

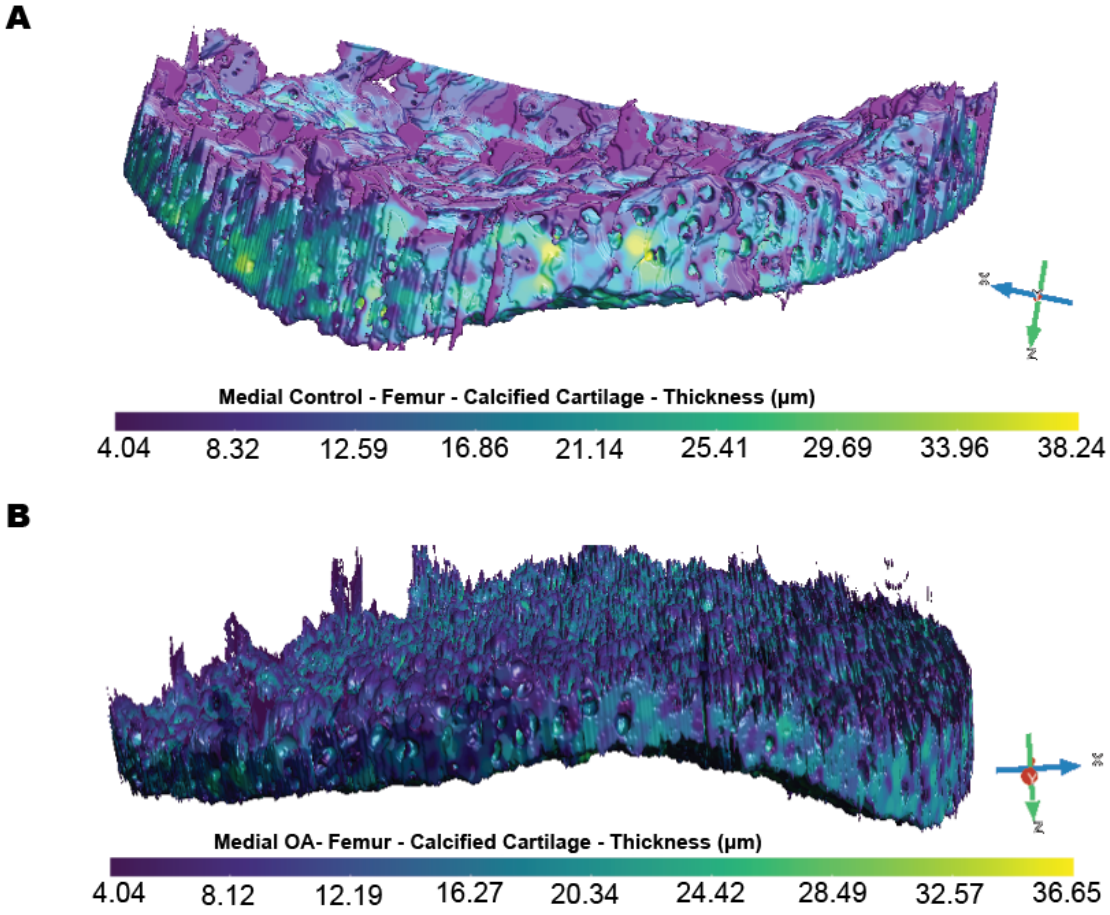

Ch. 4 – Figure 4.16. 3D visualization of medial femoral calcified cartilage thickness. *(A) Control sample shows consistent CC thickness and surface regularity. (B) OA sample shows regions of focal thinning and surface disruption. Thickness is colour coded according to the scale bar, where purple indicates lower thickness values and yellow represents greater thickness.*

To further illustrate these changes, 3D surface maps of the medial femoral CC layer were generated (Figure 5). In the control sample (Panel A), the CC layer appeared continuous and evenly distributed. In contrast, the OA sample (Panel B) showed disrupted CC morphology with clear focal thinning and irregular surface topography, further supporting localized structural remodeling.

This study found significant thinning of calcified cartilage in the medial femur and lateral tibia, with no notable changes in the medial tibia or lateral femur. These compartment-specific findings suggest that calcified cartilage remodeling in osteoarthritis may occur in a regionally distinct manner. The reduction in medial femoral calcified cartilage thickness may reflect early remodeling at the osteochondral interface, potentially driven by region specific mechanical stress. Kauppinen et al. (2019) demonstrated that changes in calcified cartilage surface topography and thickness are associated with osteoarthritis progression and correlate with histological grade and structural irregularities at the tidemark.[57] Similarly, Deng et al. (2016) reported that calcified cartilage morphology, including thinning and surface roughening, is altered in a site-specific manner during disease development.[120] The absence of significant change in the medial tibial compartment may seem unexpected, especially given the high load associated with this region in destabilization models. However, some studies have suggested that changes in calcified cartilage thickness are not solely determined by load bearing but may also depend on local remodeling dynamics and biological signaling. In contrast, the lateral tibial thinning observed here could reflect early compensatory changes or microarchitectural shifts that precede overt cartilage loss. Studies such as those by Schultz et al. (2015) have shown that calcified cartilage morphology in rodent OA models can vary between compartments, with early changes sometimes occurring in less load-bearing areas, potentially due to altered joint mechanics following injury.[121] Together, these results reinforce the idea that calcified cartilage remodeling is a complex and regionally variable process. Rather than reflecting a uniform progression, structural changes may appear first in isolated regions depending on localized mechanical, cellular, and biochemical influences.

4.4.4. Subchondral Bone Plate Thickness Stability in Early OA

To evaluate whether early osteoarthritic remodeling extended to the subchondral bone plate (SCBP), thickness measurements were performed across femoral and tibial compartments in both control and OA samples.

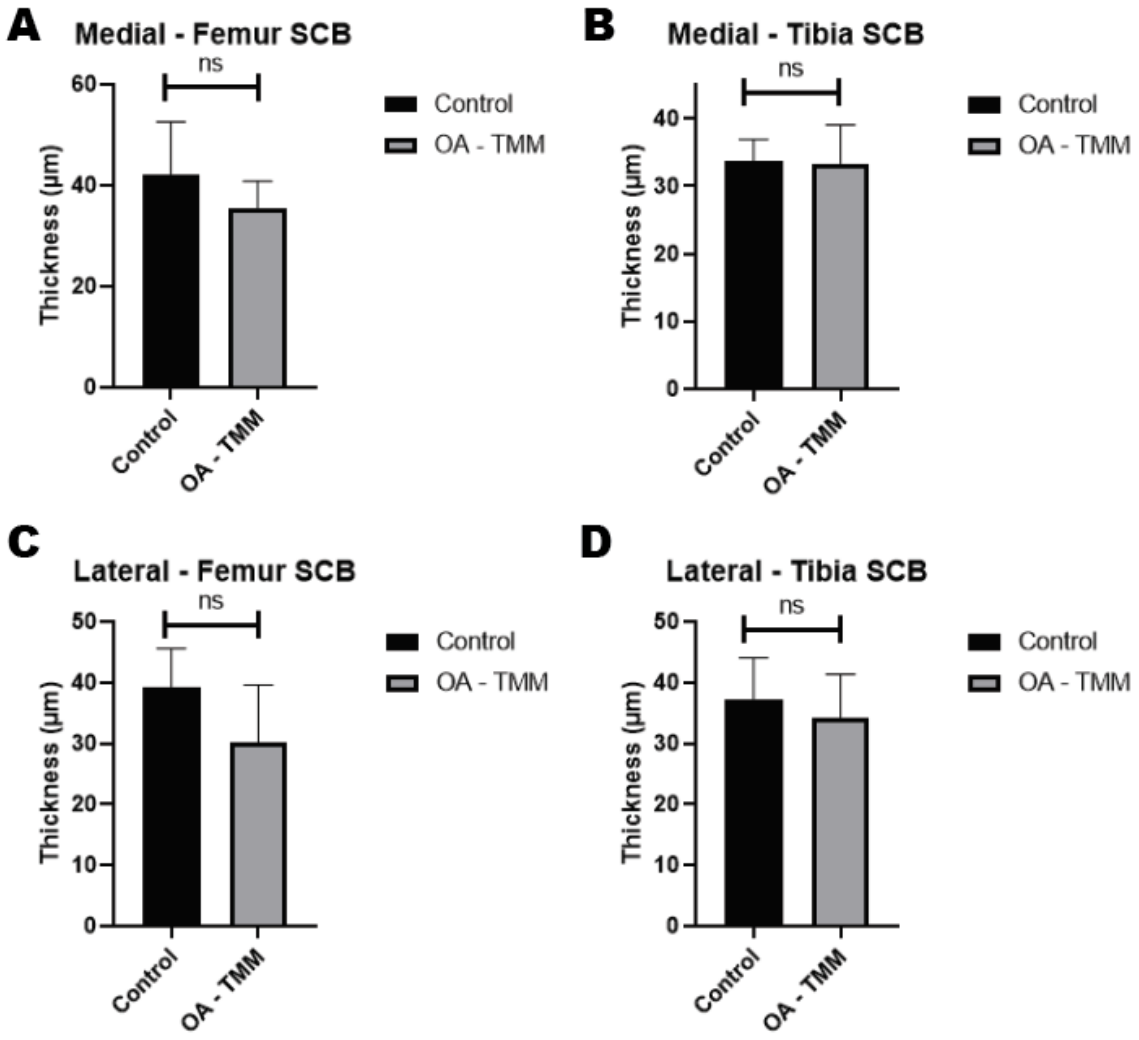

Ch. 4 – Figure 4.17. Subchondral bone plate thickness measurements across compartments. *(A–D) Thickness of subchondral bone in medial and lateral femur and tibia. All comparisons were nonsignificant.*

As shown in Figure 5, SCB thickness did not significantly differ between OA and control groups in any region examined. This includes the medial femur (Figure 5A), medial tibia (Figure 5B), lateral femur (Figure 5C), and lateral tibia (Figure 5D). Despite localized thinning in the articular and calcified cartilage layers in certain compartments, the SCBP remained structurally consistent across all anatomical sites at this early disease stage. These findings suggest that subchondral bone thickening, often associated with late-stage osteoarthritis, may not be an early hallmark of disease in this TMM-induced model. Prior studies have similarly reported that SCB sclerosis is more prominent in advanced OA, where chronic remodeling leads to increased bone mass and mineral density.[59,102] In contrast, Li et al. (2013), purposed early changes in SCB may be more functional or microstructural, such as alterations in porosity or trabecular organization, which are not captured by thickness alone.[50] The stable SCB thickness observed here supports the notion

that structural bone plate remodeling lags behind cartilage changes in the early phases of OA progression.

Nevertheless, these results reinforce the concept that cartilage degeneration precedes gross subchondral bone plate remodeling in the early stages of osteoarthritis. While the articular and calcified cartilage layers exhibit signs of regional thinning and structural disruption, the underlying subchondral bone plate remains relatively stable. This spatial and temporal degeneration highlights the complex nature of OA progression and emphasizes the importance of analyzing each tissue compartment independently. As the disease advances, future studies incorporating microarchitectural and compositional metrics may reveal more nuanced changes in subchondral bone beyond thickness alone.

4.5 Morphometric Analysis of Cortical and Trabecular Bone Alterations (Objective II)

In this section, we explore the microstructural changes in the femur and tibia of control and OA groups, with a focus on the bone volume fraction, trabecular architecture, and cortical parameters. The results presented here offer insight into how OA influences bone microarchitecture in these two critical bone regions.

4.5.1. Cortical and Trabecular Bone Volume Parameters

To evaluate potential early bone changes during osteoarthritis progression, morphometric parameters of cortical and trabecular bone were compared between OA and control groups in both the femur and tibia. Quantitative parameters included bone volume fraction (BV/TV), cortical thickness (Ct.Th), cortical area (Ct.Ar), trabecular number (Tb.N), trabecular thickness (Tb.Th), and trabecular separation (Tb.Sp).

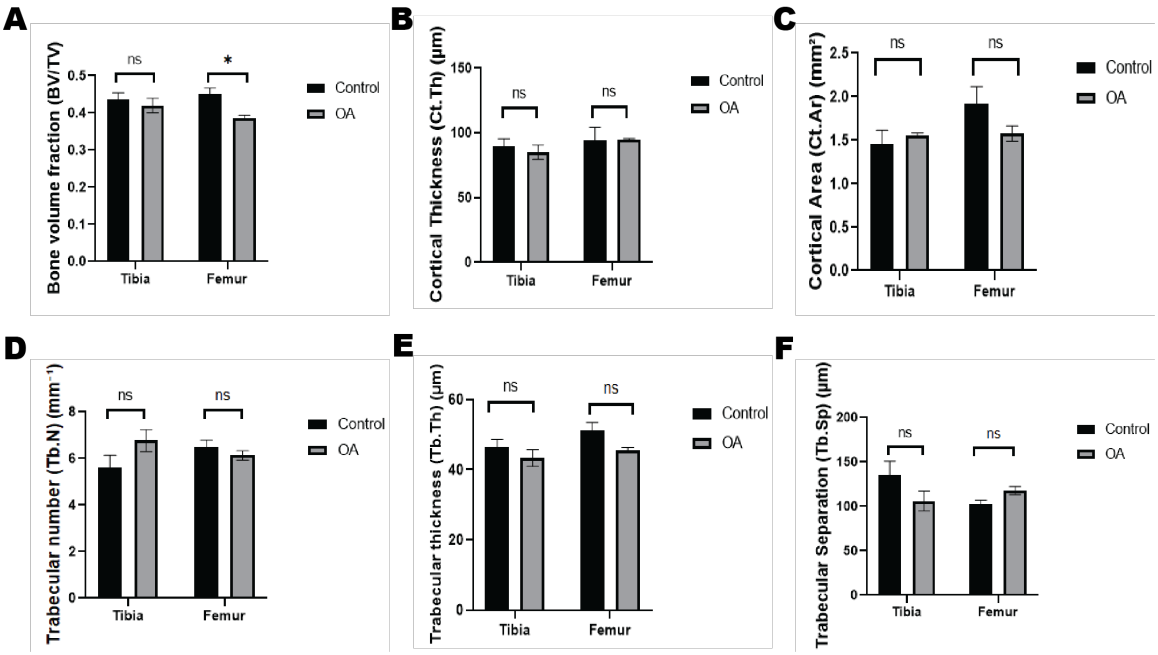

Ch. 4 – Figure 4.18. Morphometric analysis of cortical and trabecular bone parameters in the femur and tibia of control and OA groups. *(Top row) Bone volume fraction (BV/TV), cortical thickness (Ct.Th), and cortical area (Ct.Ar). (Bottom row) Trabecular number (Tb.N), trabecular thickness (Tb.Th), and trabecular separation (Tb.Sp). Data represent mean ± SD; n = 3 per group. Statistical analysis was performed using two-way ANOVA with Bonferroni correction.*

Figure 1 summarizes the mean values of these metrics and statistical comparisons between groups. A significant reduction in bone volume fraction was observed in the femur of OA samples ($p < 0.05$), indicating early bone loss in this compartment. However, tibial BV/TV remained unchanged between groups. No statistically significant changes were detected in other cortical or trabecular parameters in either bone.

Ch. 4.5 – Table 1. Comparison of microarchitecture in the femur OA and Control groups.

Microstructure	Control, mean ± SD	OA, mean ± SD
Anisotropy (MIL)	0.62 ± 0.03	0.56 ± 0.04
Anisotropy (SVD)	0.51 ± 0.02	0.50 ± 0.01
Bone surface density (BS/TV) (μm^{-1})	0.012 ± 0.001	0.010 ± 0.001
Bone volume fraction (BV/TV) (%)	0.45 ± 0.04	0.39 ± 0.03
Average cortical area (Ct.Ar) (mm^2)	1.92 ± 0.15	1.53 ± 0.17
Average cortical area fraction (Ct.Ar/Tt.Ar)	0.43 ± 0.02	0.43 ± 0.03
Cortical porosity (Ct.Po)	0.74 ± 0.05	0.76 ± 0.06
Average cortical thickness (Ct.Th) (μm)	94.30 ± 4.21	94.66 ± 5.07
Structure model index (SMI)	3.68 ± 0.30	2.47 ± 0.35
Trabecular number (Tb.N) (mm^{-1})	6.52 ± 0.41	6.13 ± 0.38
Average trabecular separation (Tb.Sp) (μm)	102.70 ± 7.66	117.77 ± 9.21
Average trabecular thickness (Tb.Th) (μm)	51.26 ± 3.44	45.61 ± 2.71
Average total (cortical + marrow) area (Tt.Ar) (mm^2)	4.44 ± 0.23	3.71 ± 0.26

Ch. 4.5 – Table 2. Comparison of microarchitecture in the tibia OA and Control groups.

Microstructure	Control, mean ± SD	OA, mean ± SD
Anisotropy (MIL)	0.63 ± 0.05	0.51 ± 0.07
Anisotropy (SVD)	0.79 ± 0.06	0.53 ± 0.08
Bone surface density (BS/TV) (μm^{-1})	0.011 ± 0.001	0.012 ± 0.001
Bone volume fraction (BV/TV) (%)	0.436 ± 0.03	0.42 ± 0.04
Average cortical area (Ct.Ar) (mm^2)	1.453 ± 0.14	1.59 ± 0.17
Average cortical area fraction (Ct.Ar/Tt.Ar)	0.447 ± 0.03	0.46 ± 0.02
Cortical porosity (Ct.Po)	0.72 ± 0.05	0.74 ± 0.06
Average cortical thickness (Ct.Th) (μm)	89.34 ± 5.32	85.18 ± 6.11
Structure model index (SMI)	4.83 ± 0.39	3.76 ± 0.44
Trabecular number (Tb.N) (mm^{-1})	5.60 ± 0.49	6.76 ± 0.54
Average trabecular separation (Tb.Sp) (μm)	135.37 ± 11.23	105.94 ± 9.88
Average trabecular thickness (Tb.Th) (μm)	46.44 ± 3.25	43.34 ± 2.97
Average total (cortical + marrow) area (Tt.Ar) (mm^2)	3.25 ± 0.21	3.36 ± 0.19

Detailed numeric comparisons of bone parameters for the femur and tibia are provided in Ch. 4.5 – Table 1 and Ch. 4.5 – Table 2, respectively. In the femur (Table 1), the OA group showed a modest decrease in bone volume fraction (0.39 ± 0.02) compared to controls (0.45 ± 0.03), which is consistent with the significant difference visualized in Figure 6. Other measures such as cortical thickness, cortical area, and trabecular morphology (e.g., Tb.N, Tb.Th, Tb.Sp) remained largely unchanged. Similarly, in the tibia (Table 2), no significant differences in cortical or trabecular parameters were observed between OA and control samples.

The observed reduction in femoral bone volume fraction suggests localized trabecular bone loss as a potential early response to mechanical and biological changes induced by OA. This aligns with previous studies demonstrating that bone structural changes, particularly in the femur, can occur in response to both pathological and aging-related stimuli. For example, Shim et al. (2022) observed pronounced age-related deterioration in femoral trabecular architecture in mice, suggesting that the femur is particularly sensitive to systemic or local changes in bone metabolism and mechanical strain.[122] Likewise, Tu et al. (2015) reported that aging mice with osteoporotic-like bone remodeling exhibited substantial alterations in femoral trabecular morphology, including increased trabecular segment radius and bone mineral density at the distal metaphysis, reinforcing the site-specific nature of trabecular remodeling.[123]

However, the lack of changes in trabecular microstructure in other compartments, including the tibia, highlights the compartment-specific nature of bone adaptation. Botter et al. (2011) similarly found that while early OA induced transient bone loss in certain compartments, structural remodeling was not uniform across the joint.[124] This spatial disparity could reflect differences in vascularity, loading environments, or the timing of cartilage and bone changes within each region.

Moreover, cortical bone metrics, including cortical thickness (Ct.Th) and cortical area (Ct.Ar), remained stable in both femur and tibia. These findings align with those of Auger et al. (2021) which observed increased cortical thickness, area, and porosity in human femoral necks with progressively severe radiographic OA, alongside decreased cortical bone mineral density (Ct.BMD).[125] Their findings suggest that cortical remodeling, particularly porosity-driven density loss, is closely tied to chronic joint degeneration and is not a prominent feature of early OA. These results suggest that in the early phases of OA, as modeled by TMM-induced joint destabilization, cartilage and calcified cartilage layers undergo more immediate structural changes, while bone adaptations may lag behind or be confined to subtle volumetric loss.

4.6 Discussion of Results

The objective of this study was to investigate early-stage osteoarthritis (OA) related changes in knee joint microstructure, with a specific focus on cellular and tissue-level remodeling across bone and cartilage compartments. Utilizing high-resolution phase contrast X-ray microscopy (XRM) alongside deep learning-based segmentation, we achieved detailed three-dimensional visualizations and quantitative analyses of articular cartilage (AC), calcified cartilage (CC), subchondral bone plate (SCBP), and both cortical and trabecular bone. The results collectively underscore the value of XRM in detecting early OA related alterations, even in the absence of significant early structural changes, and highlight the compartment and region-specific nature of OA progression.

The implementation of phase contrast XRM drastically improved visualization of soft tissue structures without the need for staining or destructive processing, in agreement with previous findings by Broche et al. (2021) and Lee et al. (2010), who demonstrated the value of propagation-based phase contrast in revealing cartilage and ligament structures otherwise poorly visualized with traditional absorption imaging.[103,104] By optimizing source-to-detector distance, this study enhanced contrast at soft tissue interfaces, enabling precise segmentation of AC and CC. Equally important was the use of deep learning-based segmentation with Dragonfly's Attention U-Net, which allowed accurate delineation of cellular features such as chondrocytes and osteocytes. This approach substantially outperformed manual segmentation or conventional thresholding methods, as previously observed in MRI-based cartilage segmentation by Zhang et al. (2018) and OA feature detection by Kumar et al. (2019).[106,107] Furthermore, the integration of watershed transformation and distance mapping enabled accurate identification and quantification of cellular features, crucial for evaluating depth-dependent morphology and spatial reorganization, which are known to occur early in OA pathogenesis.

Contrary to the hypothesis of hypertrophic osteocyte responses during early OA, our study identified a statistically significant reduction in osteocyte cell volume in one OA sample, with no consistent trends across the remaining samples. While not uniformly conclusive, this reduction aligns with reports by Tiede-Lewis et al. (2017), who described osteocyte shrinkage as part of aging-related bone remodeling, potentially reflecting early adaptive responses rather than pathology-driven hypertrophy.[109] Moreover, osteocyte spatial distribution showed a clear shift toward the subchondral region in OA samples, despite the absence of significant differences in lacunar volume or density. This depth-dependent redistribution may indicate mechanical compensation in response to altered load environments at the osteochondral interface, a concept well-supported by Palacio-Mancheno et al. (2014) and Burr and Gallant (2012), who reported similar shifts in osteocyte alignment and positioning under modified mechanical strain.[30,111] Collectively, these results suggest that early stage OA triggers local changes in bone cell structure before larger-scale bone remodeling begins.

Chondrocyte hypertrophy is considered a hallmark of OA progression, typically accompanied by upregulation of matrix metalloproteinases and type X collagen.[114] Surprisingly, our data did not reveal significant increases in chondrocyte cell volume in OA samples, suggesting that volumetric expansion may not yet be apparent at the examined disease stage. Instead, chondrocyte redistribution toward the superficial calcified cartilage layers was evident, echoing previous observations by Tschaikowsky et al. (2022), who described superficial-to-deep zone shifts as early indicators of cartilage remodeling.[116] These changes likely represent the initial stages of chondrocyte disorganization, which precede hypertrophy and contribute to subsequent matrix degradation. The preserved chondrocyte sphericity across all groups suggests that geometric remodeling of these cells is not a prominent feature of early OA. This is in line with Rim et al. (2020), who showed that significant shape distortions emerge during more advanced phases of the disease, when chondrocyte senescence and hypertrophy coincide with matrix breakdown and surface fibrillation.[117] Thus, our findings reinforce a progressive model of chondrocyte changes as shifts in position occur before changes in size, shape, or structure.

Tissue-level analysis revealed distinct region-specific changes in AC and CC, with statistically significant thinning of the medial tibial AC and medial femoral CC in OA samples. These findings align with the known mechanical vulnerability of the medial tibial plateau in destabilization models such as the TMM model used in this study, where compressive stress becomes concentrated post-meniscectomy.[15] Similarly, Kauppinen et al. (2019) reported localized thinning and roughening of the CC layer as early structural signatures of OA progression, particularly in areas of high mechanical loading.[57] Unexpectedly, the lateral tibial CC also showed significant thinning in OA, despite being a less load-bearing region. This finding may reflect early compensatory remodeling or secondary alterations in joint mechanics following meniscal destabilization, consistent with Schultz et al. (2015), who described early CC changes in less-loaded compartments of rodent OA models.[121] In contrast, SCBP thickness remained stable across all compartments, suggesting that bone plate thickening, commonly associated with advanced OA, is not a reliable indicator at early time points, a conclusion supported by Li et al. (2013) and others.[50]

Finally, morphometric analysis revealed a significant reduction in femoral trabecular bone volume fraction (BV/TV) in OA samples, with other cortical and trabecular parameters remaining largely unchanged. This femur-specific bone loss aligns with findings by Shim et al. (2022) and Tu et al. (2015), who supported the idea that the femur is especially sensitive to biological and mechanical changes, likely due to the adaptive nature of its trabecular bone structure.[122,123] In contrast, the tibia showed no significant bone changes, highlighting the spatial and temporal variability of bone remodeling in OA. Importantly, cortical parameters such as thickness, area, and porosity were unaffected in both datsets. These findings suggest that cortical bone remodeling may occur later in disease progression, as supported by Auger et al. (2021), who noted significant cortical alterations only in advanced stages of OA.[125] The preservation of cortical geometry further supports the idea that cartilage and CC degeneration precede new bone responses, a model

consistent with the temporally staged progression of OA described by Botter et al. (2011).[124]

This study confirms that XRM, in combination with deep learning segmentation, enables the high-resolution, non-destructive analysis of subtle OA-induced alterations across joint tissues. Early-stage OA appears to be characterized by region-specific cartilage thinning, superficial cellular redistribution, and selective trabecular bone loss, without widespread structural degeneration in cortical bone or the SCBP. These compartmentalized and temporally nuanced responses highlight the need for sensitive imaging and analysis tools capable of detecting early changes before irreversible joint degradation occurs.

Chapter 5: Conclusions & Future Work

In this thesis, high-resolution X-ray microscopy (XRM) combined with deep learning segmentation has been demonstrated as a powerful and non-destructive approach for the three-dimensional quantification of microstructural and cellular changes in early-stage osteoarthritis (OA). By leveraging propagation-based phase contrast imaging and advanced object-based morphometry in Dragonfly, this work provides new insight into the spatial and depth-dependent alterations of osteocyte and chondrocyte morphology in a surgically induced OA mouse model. The methods developed here facilitate visualization of soft and mineralized tissues at near-histological resolution, with the added benefit of preserving the native architecture across intact femur–tibia joint complexes.

5.1. Quantification of Cellular Changes: Osteocyte and Chondrocyte Volume and Depth-Dependent Variations

This thesis established a 3D deep learning-based workflow for the segmentation and quantification of osteocytes and chondrocytes in the femoral and tibial compartments of the mouse knee joint. Using high-resolution XRM and attention U-Net segmentation, we identified that early-stage OA induces distinct changes in cell morphology and spatial organization. Osteocyte volume and distribution showed region-specific alterations in the femur of OA joints, suggesting localized bone remodeling responses that precede large-scale structural changes. Meanwhile, chondrocyte analysis revealed significant shifts in volume and vertical distribution within calcified cartilage, particularly in the medial femoral region, without concurrent loss of sphericity. These results support a model where early OA involves spatial reorganization and hypertrophic changes in cartilage-resident cells before overt degeneration.

Limitations: While this study provides novel insights into early cellular remodeling, the analysis was based on a small sample size (n = 3 per group), which limits statistical power. Additionally, the analysis involved manual declination and watershed transformation during the segmentation pipeline, which is not always 100% accurate. Particularly for densely packed or overlapping cells, it is challenging to reliably distinguish one object per individual cell, potentially leading to over or under segmentation in some regions.

Future work: Future studies should aim to improve the accuracy of cell segmentation by refining the deep learning pipeline, particularly for distinguishing closely packed or overlapping cells. Expanding the sample size and including earlier and later disease time points would help capture a more complete picture of cellular remodeling over time. Additionally, integrating other morphological features such as elongation, orientation, or cell clustering could offer a more comprehensive view of how chondrocytes and osteocytes respond to early joint degeneration.

5.2. Remodeling of the Osteochondral Interface: Articular Cartilage, Calcified Cartilage, and Subchondral Bone Plate

This study quantitatively assessed early-stage remodeling at the osteochondral interface by measuring the thickness of articular cartilage, calcified cartilage, and the subchondral bone plate. Using phase-contrast XRM imaging and 3D segmentation in Dragonfly, regional changes were captured across medial and lateral compartments of the femur and tibia. The findings revealed localized thinning of the articular cartilage and thickening of calcified cartilage in early OA, particularly within medial regions subject to increased mechanical loading. In contrast, subchondral bone plate thickness remained relatively stable between control and OA groups, perhaps indicating that bone remodeling at this early stage is largely restricted to the cartilage layers.

These results support a compartment-specific model of joint degeneration, where early morphological changes occur in calcified cartilage and articular cartilage before overt subchondral bone alterations. The ability to visualize and quantify such subtle tissue level differences highlights the usage of high-resolution XRM for early OA research.

Limitations: This analysis was limited by the resolution and accuracy of segmentation at tissue boundaries, especially in thin regions like articular cartilage. Manual correction was required to verify boundaries between cartilage and bone, introducing some manual dependency. Additionally, the small sample size and short disease duration may not fully capture longer-term changes in bone plate remodeling or mineralization**.**

Future work: Future work should incorporate time course studies to evaluate progressive changes across the osteochondral interface and extend analyses to include mineral density or collagen orientation to better understand tissue quality. Integration with histology could also help validate and complement 3D XRM findings, improving the biological interpretation of remodeling dynamics at the cartilage–bone interface.

5.3. Comprehensive Assessment of Cortical and Trabecular Bone Microarchitecture

In Chapter 4, detailed morphometric analysis of cortical and trabecular bone architecture in femoral and tibial compartments revealed early osteoarthritic changes with regional specificity. High-resolution XRM and deep learning-based segmentation enabled quantification of trabecular thickness, separation, number, and cortical thickness and area. Cortical bone in the femur showed notable changes in the OA group, indicating localized remodeling in response to joint instability, while the tibial bone remained largely unchanged. These results could highlight the compartment-specific nature of bone adaptation and the importance of site-specific evaluation in early-stage OA.

Limitations: A key limitation lies in the use of the Bone Analysis plugin for morphometric quantification. As a semi-automated tool with limited transparency in its internal processing, particularly for complex 3D geometries, there is inherent uncertainty in how certain parameters are computed. Moreover, sensitivity to segmentation thresholds and parameter tuning can introduce variability across samples, potentially influencing the reproducibility and precision of the extracted metrics.

Future Work: Future analyses could benefit from refining the morphometric pipeline to increase transparency and control over segmentation parameters, particularly for distinguishing complex 3D structures. Incorporating open source or fully customizable tools may enhance reproducibility and reduce uncertainty. Additionally, while this study assessed the entire femur and tibia, including regions above and below the growth plate, many previous studies have focused solely on the metaphysis or epiphysis. Future work could leverage this broader anatomical coverage to explore region-specific differences in bone remodeling and their relationship to localized joint degeneration in early-stage OA. Comparing specific femoral and tibial regions can reveal local changes and loading responses that standard methods might overlook.

5.4. Deep Learning-Based Segmentation for Enhanced Joint Tissue Analysis

This work implemented an Attention U-Net deep learning model to perform high-resolution segmentation of joint tissues, enabling detailed quantification of cellular and structural changes in osteoarthritis. The model successfully distinguished key anatomical features, including articular cartilage, calcified cartilage, subchondral bone, chondrocytes, and osteocytes, providing a novel platform for morphometric and spatial analysis. By combining orthogonal and 3D visualizations in Dragonfly with manual annotations for model training, the pipeline enabled anatomically detailed segmentation across joint tissues This approach provided a scalable and efficient alternative to fully manual processing, allowing for high-resolution cellular analysis of early OA changes while minimizing processing time.

Limitations: Despite its efficiency, the segmentation approach has limitations. Manual delineation of training data introduces subjectivity, and the watershed-based object separation struggles to consistently identify individual cells in densely packed regions, leading to potential over or under segmentation. Additionally, the attention U-Net model, while effective, depends heavily on the quality and diversity of the training slices, which may limit generalizability across anatomical regions or datasets with different contrast or resolution characteristics.

Future work: Future directions should focus on enhancing segmentation accuracy by exploring alternative segmentation models and comparing their performance against the current deep learning approach. In addition, integrating other image analysis platforms

such as Fiji could help validate segmentation outputs and improve confidence in quantitative measurements. Expanding the annotated dataset across more anatomical regions and OA timepoints would also improve the model's adaptability. Finally, incorporating multi-class segmentation for cell types, tissue zones, and extracellular components could enable a more detailed and integrative assessment of OA bone remodelling.

References:

1. CJRR annual report: Hip and knee replacements in Canada, 2018–2019 | CIHI. https://www.cihi.ca/en/cjrr-annual-report-hip-and-knee-replacements-in-canada-2018-2019.
2. Mora, J. C., Przkora, R. & Cruz-Almeida, Y. Knee osteoarthritis: pathophysiology and current treatment modalities. *J Pain Res* **11**, 2189–2196 (2018).
3. Canada, P. H. A. of. Osteoarthritis in Canada. https://www.canada.ca/en/public-health/services/publications/diseases-conditions/osteoarthritis.html (2020).
4. Hip and Knee Replacements in Canada: CJRR Annual Statistics Summary, 2018–2019.
5. Oei, E. H. G. & Runhaar, J. Imaging of early-stage osteoarthritis: the needs and challenges for diagnosis and classification. *Skeletal Radiol* **52**, 2031–2036 (2023).
6. Eckstein, F. *et al.* Imaging of cartilage and bone: promises and pitfalls in clinical trials of osteoarthritis. *Osteoarthritis Cartilage* **22**, 1516–1532 (2014).
7. Vomer, R. P., Boggess, S. & Boggess, B. Ultrasound Evaluation of Knee Osteoarthritis. *Cureus* **15**, e39188.
8. Roemer, F. W., Guermazi, A., Demehri, S., Wirth, W. & Kijowski, R. Imaging in Osteoarthritis. *Osteoarthritis and Cartilage* **30**, 913–934 (2022).
9. Nieminen, H. J. *et al.* 3D histopathological grading of osteochondral tissue using contrast-enhanced micro-computed tomography. *Osteoarthritis Cartilage* **25**, 1680–1689 (2017).

10. Gahunia, H. *et al.* 3D-histopathological grading of articular cartilage using contrast-enhanced high-resolution micro-CT. *Osteoarthritis and Cartilage* **24**, S277–S278 (2016).
11. Zhu, Y., Manske, S. L. & Boyd, S. K. Cartilage imaging of a rabbit knee using dual-energy X-ray microscopy and 1.0 T and 9.4 T magnetic resonance imaging. *J Orthop Translat* **3**, 212–218 (2015).
12. Tang, T. *et al.* Characterization of human trabecular bone across multiple length scales using a correlative approach combining X-ray tomography with LaserFIB and plasma FIB-SEM. *Sci Rep* **14**, 21604 (2024).
13. Duncan, K. E., Czymmek, K. J., Jiang, N., Thies, A. C. & Topp, C. N. X-ray microscopy enables multiscale high-resolution 3D imaging of plant cells, tissues, and organs. *Plant Physiol* **188**, 831–845 (2022).
14. Fang, H. *et al.* Early Changes of Articular Cartilage and Subchondral Bone in The DMM Mouse Model of Osteoarthritis. *Sci Rep* **8**, 2855 (2018).
15. Glasson, S. S., Blanchet, T. J. & Morris, E. A. The surgical destabilization of the medial meniscus (DMM) model of osteoarthritis in the 129/SvEv mouse. *Osteoarthritis Cartilage* **15**, 1061–1069 (2007).
16. Lorenz, J. & Grässel, S. Experimental Osteoarthritis Models in Mice. in *Mouse Genetics: Methods and Protocols* (eds. Singh, S. R. & Coppola, V.) 401–419 (Springer, New York, NY, 2014). doi:10.1007/978-1-4939-1215-5_23.
17. Nagai-Tanima, M., Ishikawa, A., Ishida, K., Takakuwa, T. & Aoyama, T. THE KINEMATIC ANALYSIS OF ANTERIOR CRUCIATE LIGAMENT-

TRANSECTION MODEL AND RE STABILIZED MODEL. *Osteoarthritis and Cartilage* **30**, S153–S154 (2022).

18. Hunter, D. J. & Bierma-Zeinstra, S. Osteoarthritis. *The Lancet* **393**, 1745–1759 (2019).
19. Longobardi, L. *et al.* Role of the C-C chemokine receptor-2 in a murine model of injury-induced osteoarthritis. *Osteoarthritis and Cartilage* **25**, 914–925 (2017).
20. Loeser, R. F., Goldring, S. R., Scanzello, C. R. & Goldring, M. B. Osteoarthritis: A disease of the joint as an organ. *Arthritis & Rheumatism* **64**, 1697–1707 (2012).
21. Steinmetz, J. D. *et al.* Global, regional, and national burden of osteoarthritis, 1990–2020 and projections to 2050: a systematic analysis for the Global Burden of Disease Study 2021. *The Lancet Rheumatology* **5**, e508–e522 (2023).
22. Cross, M. *et al.* The global burden of hip and knee osteoarthritis: estimates from the global burden of disease 2010 study. *Ann Rheum Dis* **73**, 1323–1330 (2014).
23. Vincent, K. R., Conrad, B. P., Fregly, B. J. & Vincent, H. K. The Pathophysiology of Osteoarthritis: A Mechanical Perspective on the Knee Joint. *PM R* **4**, S3–S9 (2012).
24. Sharma, L. *et al.* Varus and Valgus Alignment and Incident and Progressive Knee Osteoarthritis. *Ann Rheum Dis* **69**, 1940–1945 (2010).
25. Mobasheri, A. & Batt, M. An update on the pathophysiology of osteoarthritis. *Annals of Physical and Rehabilitation Medicine* **59**, 333–339 (2016).

26. Vincent, T. L., McClurg, O. & Troeberg, L. The Extracellular Matrix of Articular Cartilage Controls the Bioavailability of Pericellular Matrix-Bound Growth Factors to Drive Tissue Homeostasis and Repair. *Int J Mol Sci* **23**, 6003 (2022).

27. Poulet, B. & Staines, K. A. New developments in osteoarthritis and cartilage biology. *Curr Opin Pharmacol* **28**, 8–13 (2016).

28. Goldring, M. B. *et al.* Roles of inflammatory and anabolic cytokines in cartilage metabolism: signals and multiple effectors converge upon MMP-13 regulation in osteoarthritis. *Eur Cell Mater* **21**, 202–220 (2011).

29. Hu, Q. & Ecker, M. Overview of MMP-13 as a Promising Target for the Treatment of Osteoarthritis. *International Journal of Molecular Sciences* **22**, 1742 (2021).

30. Burr, D. B. & Gallant, M. A. Bone remodelling in osteoarthritis. *Nat Rev Rheumatol* **8**, 665–673 (2012).

31. Solanki, K., Shanmugasundaram, S., Shetty, N. & Kim, S.-J. Articular cartilage repair & joint preservation: A review of the current status of biological approach. *J Clin Orthop Trauma* **22**, 101602 (2021).

32. Scanzello, C. R. & Goldring, S. R. The Role of Synovitis in Osteoarthritis pathogenesis. *Bone* **51**, 249–257 (2012).

33. Sanchez-Lopez, E., Coras, R., Torres, A., Lane, N. E. & Guma, M. Synovial inflammation in osteoarthritis progression. *Nat Rev Rheumatol* **18**, 258–275 (2022).

34. Molnar, V. *et al.* Cytokines and Chemokines Involved in Osteoarthritis Pathogenesis. *Int J Mol Sci* **22**, 9208 (2021).

35. De Roover, A., Escribano-Núñez, A., Monteagudo, S. & Lories, R. Fundamentals of osteoarthritis: Inflammatory mediators in osteoarthritis. *Osteoarthritis and Cartilage* **31**, 1303–1311 (2023).

36. van der Kraan, P. M. & van den Berg, W. B. Chondrocyte hypertrophy and osteoarthritis: role in initiation and progression of cartilage degeneration? *Osteoarthritis Cartilage* **20**, 223–232 (2012).

37. Dreier, R. Hypertrophic differentiation of chondrocytes in osteoarthritis: the developmental aspect of degenerative joint disorders. *Arthritis Res Ther* **12**, 216 (2010).

38. Sharma, A. R., Jagga, S., Lee, S.-S. & Nam, J.-S. Interplay between Cartilage and Subchondral Bone Contributing to Pathogenesis of Osteoarthritis. *Int J Mol Sci* **14**, 19805–19830 (2013).

39. Little, C. B. & Hunter, D. J. Post-traumatic osteoarthritis: from mouse models to clinical trials. *Nat Rev Rheumatol* **9**, 485–497 (2013).

40. Staines, K. A., Poulet, B., Wentworth, D. N. & Pitsillides, A. A. The STR/ort mouse model of spontaneous osteoarthritis – an update. *Osteoarthritis Cartilage* **25**, 802–808 (2017).

41. Pitcher, T., Sousa-Valente, J. & Malcangio, M. The Monoiodoacetate Model of Osteoarthritis Pain in the Mouse. *J Vis Exp* 53746 (2016) doi:10.3791/53746.

42. Bansal, S. *et al.* Transection of the medial meniscus anterior horn results in cartilage degeneration and meniscus remodeling in a large animal model. *J Orthop Res* **38**, 2696–2708 (2020).

43. Hoemann, C. D., Lafantaisie-Favreau, C.-H., Lascau-Coman, V., Chen, G. & Guzmán-Morales, J. The cartilage-bone interface. *J Knee Surg* **25**, 85–97 (2012).

44. Sophia Fox, A. J., Bedi, A. & Rodeo, S. A. The basic science of articular cartilage: structure, composition, and function. *Sports Health* **1**, 461–468 (2009).

45. Buckwalter, J. A. & Mankin, H. J. Articular cartilage: tissue design and chondrocyte-matrix interactions. *Instr Course Lect* **47**, 477–486 (1998).

46. Makris, E. A., Gomoll, A. H., Malizos, K. N., Hu, J. C. & Athanasiou, K. A. Repair and tissue engineering techniques for articular cartilage. *Nat Rev Rheumatol* **11**, 21–34 (2015).

47. Madi, K. *et al.* In situ characterization of nanoscale strains in loaded whole joints via synchrotron X-ray tomography. *Nat Biomed Eng* **4**, 343–354 (2020).

48. Chen, N., Wu, R. W. H., Lam, Y., Chan, W. C. W. & Chan, D. Hypertrophic chondrocytes at the junction of musculoskeletal structures. *Bone Rep* **19**, 101698 (2023).

49. Jeon, O. H. *et al.* Local clearance of senescent cells attenuates the development of post-traumatic osteoarthritis and creates a pro-regenerative environment. *Nat Med* **23**, 775–781 (2017).

50. Li, G. *et al.* Subchondral bone in osteoarthritis: insight into risk factors and microstructural changes. *Arthritis Res Ther* **15**, 223 (2013).

51. Findlay, D. M. & Kuliwaba, J. S. Bone–cartilage crosstalk: a conversation for understanding osteoarthritis. *Bone Res* **4**, 1–12 (2016).

52. Feng, X. Chemical and Biochemical Basis of Cell-Bone Matrix Interaction in Health and Disease. *Curr Chem Biol* **3**, 189–196 (2009).

53. Kurzyk, A. *et al.* Calcination and ion substitution improve physicochemical and biological properties of nanohydroxyapatite for bone tissue engineering applications. *Sci Rep* **13**, 15384 (2023).

54. Hart, N. H. *et al.* Biological basis of bone strength: anatomy, physiology and measurement. *J Musculoskelet Neuronal Interact* **20**, 347–371 (2020).

55. Tat, S. K., Lajeunesse, D., Pelletier, J.-P. & Martel-Pelletier, J. Targeting subchondral bone for treating osteoarthritis: what is the evidence? *Best Pract Res Clin Rheumatol* **24**, 51–70 (2010).

56. Burr, D. B. Anatomy and physiology of the mineralized tissues: Role in the pathogenesis of osteoarthrosis. *Osteoarthritis and Cartilage* **12**, 20–30 (2004).

57. Kauppinen, S. *et al.* 3D morphometric analysis of calcified cartilage properties using micro-computed tomography. *Osteoarthritis and Cartilage* **27**, 172–180 (2019).

58. Oftadeh, R., Perez-Viloria, M., Villa-Camacho, J. C., Vaziri, A. & Nazarian, A. Biomechanics and Mechanobiology of Trabecular Bone: A Review. *J Biomech Eng* **137**, 0108021–01080215 (2015).

59. Hayami, T. *et al.* The role of subchondral bone remodeling in osteoarthritis: reduction of cartilage degeneration and prevention of osteophyte formation by alendronate in the rat anterior cruciate ligament transection model. *Arthritis Rheum* **50**, 1193–1206 (2004).

60. Olivares-Navarrete, R. *et al.* Substrate Stiffness Controls Osteoblastic and Chondrocytic Differentiation of Mesenchymal Stem Cells without Exogenous Stimuli. *PLOS ONE* **12**, e0170312 (2017).

61. Bonewald, L. F. The amazing osteocyte. *J Bone Miner Res* **26**, 229–238 (2011).

62. Tiede-Lewis, L. M. & Dallas, S. L. Changes in the Osteocyte Lacunocanalicular Network with Aging. *Bone* **122**, 101–113 (2019).

63. Milovanovic, P. *et al.* Osteocytic canalicular networks: morphological implications for altered mechanosensitivity. *ACS Nano* **7**, 7542–7551 (2013).

64. Hemmatian, H., Bakker, A. D., Klein-Nulend, J. & van Lenthe, G. H. Aging, Osteocytes, and Mechanotransduction. *Curr Osteoporos Rep* **15**, 401–411 (2017).

65. Li, Q., Amano, K., Link, T. M. & Ma, C. B. Advanced Imaging in Osteoarthritis. *Sports Health* **8**, 418–428 (2016).

66. Guermazi, A. *et al.* Compositional MRI techniques for evaluation of cartilage degeneration in osteoarthritis. *Osteoarthritis and Cartilage* **23**, 1639–1653 (2015).

67. Edelstein, W. A., Mahesh, M. & Carrino, J. A. MRI: Time Is Dose—and Money and Versatility. *J Am Coll Radiol* **7**, 650–652 (2010).

68. Ali, T. S., Prasadam, I., Xiao, Y. & Momot, K. I. Progression of Post-Traumatic Osteoarthritis in rat meniscectomy models: Comprehensive monitoring using MRI. *Sci Rep* **8**, 6861 (2018).

69. Luo, P. *et al.* Enabling early detection of knee osteoarthritis using diffusion-relaxation correlation spectrum imaging. *Clin Radiol* **78**, e681–e687 (2023).

70. Mandl, P. *et al.* Ultrasound evaluation of fluid in knee recesses at varying degrees of flexion. *Arthritis Care Res (Hoboken)* **64**, 773–779 (2012).

71. Nieminen, H. J., Salmi, A., Karppinen, P., Hæggström, E. & Hacking, S. A. The potential utility of high-intensity ultrasound to treat osteoarthritis. *Osteoarthritis and Cartilage* **22**, 1784–1799 (2014).

72. Jia, Q., Xu, H., Wang, T., Liang, Q. & Wu, L. In vivo quantification of collagen-induced arthritis mouse model by three-dimensional volumetric ultrasound and color Doppler. *PLoS One* **20**, e0321124 (2025).

73. Filippucci, E. *et al.* Ultrasound imaging for the rheumatologist VII. Ultrasound imaging in rheumatoid arthritis. *Clin Exp Rheumatol* **25**, 5–10 (2007).

74. Zhang, H. *et al.* Research progress of ultrasound in accurate evaluation of cartilage injury in osteoarthritis. *Front Endocrinol (Lausanne)* **15**, 1420049 (2024).

75. Tan, M. T. & Lloyd, T. B. Utility of dual energy computed tomography in the evaluation of infiltrative skeletal lesions and metastasis: a literature review. *Skeletal Radiol* **51**, 1731–1741 (2022).

76. Eibschutz, L. S., Matcuk, G., Chiu, M. K.-J., Lu, M. Y. & Gholamrezanezhad, A. Updates on the Applications of Spectral Computed Tomography for Musculoskeletal Imaging. *Diagnostics (Basel)* **14**, 732 (2024).

77. Baer, K. *et al.* Spectral CT imaging of human osteoarthritic cartilage via quantitative assessment of glycosaminoglycan content using multiple contrast agents. *APL Bioeng* **5**, 026101 (2021).

78. Zhao, H. *et al.* Dual-energy CT virtual non-calcium: an accurate method for detection of knee osteoarthritis-related edema-like marrow signal intensity. *Insights Imaging* **14**, 74 (2023).

79. Obata, Y. *et al.* Quantitative and qualitative bone imaging: A review of synchrotron radiation microtomography analysis in bone research. *J Mech Behav Biomed Mater* **110**, 103887 (2020).

80. Peyrin, F., Dong, P., Pacureanu, A. & Langer, M. Micro- and nano-CT for the study of bone ultrastructure. *Curr Osteoporos Rep* **12**, 465–474 (2014).

81. Goff, E. *et al.* Large-scale quantification of human osteocyte lacunar morphological biomarkers as assessed by ultra-high-resolution desktop micro-computed tomography. *Bone* **152**, 116094 (2021).

82. Drevet, S., Favier, B., Lardy, B., Gavazzi, G. & Brun, E. New imaging tools for mouse models of osteoarthritis. *GeroScience* **44**, 639–650 (2022).

83. Zhu, Y., Ponjevic, D., Matyas, J. R. & Boyd, S. K. Contrast-enhanced x-ray microscopy of articular cartilage. *Connect Tissue Res* **62**, 542–553 (2021).

84. Gunaseelan, I. *et al.* Propagation-based phase-contrast imaging of the breast: image quality and the effect of X-ray energy and radiation dose. *Br J Radiol* **96**, 20221189 (2023).

85. Paganin, D., Mayo, S. C., Gureyev, T. E., Miller, P. R. & Wilkins, S. W. Simultaneous phase and amplitude extraction from a single defocused image of a homogeneous object. *Journal of Microscopy* **206**, 33–40 (2002).

86. Momose, A. Recent Advances in X-ray Phase Imaging. *Jpn. J. Appl. Phys.* **44**, 6355 (2005).

87. Appel, A., Anastasio, M. A. & Brey, E. M. Potential for Imaging Engineered Tissues with X-Ray Phase Contrast. *Tissue Eng Part B Rev* **17**, 321–330 (2011).

88. Mayo, S. C. *et al.* X-ray phase-contrast microscopy and microtomography. *Opt. Express, OE* **11**, 2289–2302 (2003).

89. Clark, J. N. *et al.* Propagation phase-contrast micro-computed tomography allows laboratory-based three-dimensional imaging of articular cartilage down to the cellular level. *Osteoarthritis and Cartilage* **28**, 102–111 (2020).

90. Kyrieleis, A., Titarenko, V., Ibison, M., Connolley, T. & Withers, P. J. Region-of-interest tomography using filtered backprojection: assessing the practical limits. *J Microsc* **241**, 69–82 (2011).

91. Koetzier, L. R. *et al.* Deep Learning Image Reconstruction for CT: Technical Principles and Clinical Prospects. *Radiology* **306**, e221257 (2023).

92. Schindelin, J. *et al.* Fiji - an Open Source platform for biological image analysis. *Nat Methods* **9**, 10.1038/nmeth.2019 (2012).

93. Ronneberger, O., Fischer, P. & Brox, T. U-Net: Convolutional Networks for Biomedical Image Segmentation. Preprint at https://doi.org/10.48550/arXiv.1505.04597 (2015).

94. Oktay, O. *et al.* Attention U-Net: Learning Where to Look for the Pancreas. Preprint at https://doi.org/10.48550/arXiv.1804.03999 (2018).

95. Schlemper, J. *et al.* Attention gated networks: Learning to leverage salient regions in medical images. *Med Image Anal* **53**, 197–207 (2019).

96. Diakogiannis, F. I., Waldner, F., Caccetta, P. & Wu, C. ResUNet-a: a deep learning framework for semantic segmentation of remotely sensed data. *ISPRS Journal of Photogrammetry and Remote Sensing* **162**, 94–114 (2020).

97. Milletari, F., Navab, N. & Ahmadi, S.-A. V-Net: Fully Convolutional Neural Networks for Volumetric Medical Image Segmentation. Preprint at https://doi.org/10.48550/arXiv.1606.04797 (2016).

98. Isensee, F., Jaeger, P. F., Kohl, S. A. A., Petersen, J. & Maier-Hein, K. H. nnU-Net: a self-configuring method for deep learning-based biomedical image segmentation. *Nat Methods* **18**, 203–211 (2021).

99. Lindblad, J. Surface area estimation of digitized 3D objects using weighted local configurations. *Image and Vision Computing* **23**, 111–122 (2005).

100. Kitchen, M. J. *et al.* CT dose reduction factors in the thousands using X-ray phase contrast. *Sci Rep* **7**, 15953 (2017).

101. Bravin, A., Coan, P. & Suortti, P. X-ray phase-contrast imaging: from pre-clinical applications towards clinics. *Phys Med Biol* **58**, R1-35 (2013).

102. Goldring, M. B. & Goldring, S. R. Articular cartilage and subchondral bone in the pathogenesis of osteoarthritis. *Ann N Y Acad Sci* **1192**, 230–237 (2010).

103. Lee, Y. S. *et al.* Articular cartilage imaging by the use of phase-contrast tomography in a collagen-induced arthritis mouse model. *Acad Radiol* **17**, 244–250 (2010).

104. Broche, L. *et al.* Calcified cartilage revealed in whole joint by X-ray phase contrast imaging. *Osteoarthritis and Cartilage Open* **3**, (2021).

105. Buie, H. R., Campbell, G. M., Klinck, R. J., MacNeil, J. A. & Boyd, S. K. Automatic segmentation of cortical and trabecular compartments based on a dual threshold technique for in vivo micro-CT bone analysis. *Bone* **41**, 505–515 (2007).

106. Zhang, B. *et al.* Computer-Aided Knee Joint Magnetic Resonance Image Segmentation - A Survey. Preprint at https://doi.org/10.48550/arXiv.1802.04894 (2018).

107. Kumar, D., Gandhamal, A., Talbar, S. & Hani, A. F. M. Knee Articular Cartilage Segmentation from MR Images: A Review. *ACM Comput. Surv.* **51**, 1–29 (2019).

108. Kim, B. J. *et al.* Establishment of a reliable and reproducible murine osteoarthritis model. *Osteoarthritis Cartilage* **21**, 2013–2020 (2013).

109. Tiede-Lewis, L. M. *et al.* Degeneration of the osteocyte network in the C57BL/6 mouse model of aging. *Aging (Albany NY)* **9**, 2190–2208 (2017).

110. Teichtahl, A. J. *et al.* Wolff's law in action: a mechanism for early knee osteoarthritis. *Arthritis Research & Therapy* **17**, 207 (2015).

111. Palacio-Mancheno, P. E., Larriera, A. I., Doty, S. B., Cardoso, L. & Fritton, S. P. 3D Assessment of Cortical Bone Porosity and Tissue Mineral Density Using High-Resolution Micro-CT: Effects of Resolution and Threshold Method. *J Bone Miner Res* **29**, 10.1002/jbmr.2012 (2014).

112. Carpentier, V. T. *et al.* Increased proportion of hypermineralized osteocyte lacunae in osteoporotic and osteoarthritic human trabecular bone: implications for bone remodeling. *Bone* **50**, 688–694 (2012).

113. Muratovic, D. *et al.* Microstructural and cellular characterisation of the subchondral trabecular bone in human knee and hip osteoarthritis using synchrotron tomography. *Osteoarthritis and Cartilage* **31**, 1224–1233 (2023).

114. Kamekura, S. *et al.* Osteoarthritis development in novel experimental mouse models induced by knee joint instability. *Osteoarthritis Cartilage* **13**, 632–641 (2005).

115. Li, H., Wang, D., Yuan, Y. & Min, J. New insights on the MMP-13 regulatory network in the pathogenesis of early osteoarthritis. *Arthritis Research & Therapy* **19**, 248 (2017).

116. Tschaikowsky, M. *et al.* The articular cartilage surface is impaired by a loss of thick collagen fibers and formation of type I collagen in early osteoarthritis. *Acta Biomaterialia* **146**, 274–283 (2022).

117. Rim, Y. A., Nam, Y. & Ju, J. H. The Role of Chondrocyte Hypertrophy and Senescence in Osteoarthritis Initiation and Progression. *International Journal of Molecular Sciences* **21**, 2358 (2020).

118. Peng, X. *et al.* Current advances in animal model of meniscal injury: From meniscal injury to osteoarthritis. *Journal of Orthopaedic Translation* **50**, 388–402 (2025).

119. Hada, S. *et al.* The degeneration and destruction of femoral articular cartilage shows a greater degree of deterioration than that of the tibial and patellar articular cartilage

in early stage knee osteoarthritis: a cross-sectional study. *Osteoarthritis and Cartilage* **22**, 1583–1589 (2014).

120. Deng, B. *et al.* Quantitative study on morphology of calcified cartilage zone in OARSI 0∼4 cartilage from osteoarthritic knees. *Curr Res Transl Med* **64**, 149–154 (2016).
121. Schultz, M., Molligan, J., Schon, L. & Zhang, Z. Pathology of the Calcified Zone of Articular Cartilage in Post-Traumatic Osteoarthritis in Rat Knees. *PLOS ONE* **10**, e0120949 (2015).
122. Shim, J., Iwaya, C., Ambrose, C. G., Suzuki, A. & Iwata, J. Micro-computed tomography assessment of bone structure in aging mice. *Sci Rep* **12**, 8117 (2022).
123. Tu, S.-J., Huang, H.-W. & Chang, W.-J. X-ray imaging characterization of femoral bones in aging mice with osteopetrotic disorder. *Micron* **71**, 14–21 (2015).
124. Botter, S. M. *et al.* Osteoarthritis induction leads to early and temporal subchondral plate porosity in the tibial plateau of mice: an in vivo microfocal computed tomography study. *Arthritis Rheum* **63**, 2690–2699 (2011).
125. Auger, J. D., Naik, A. J., Murakami, A. M., Gerstenfeld, L. C. & Morgan, E. F. Spatial assessment of femoral neck bone density and microstructure in hip osteoarthritis. *Bone Rep* **16**, 101155 (2021).